Petroleum Science 23 (2026) 1159–1181

Contents lists available at ScienceDirect

Petroleum Science

journal homepage: www.keaipublishing.com/en/journals/petroleum-science

Original Paper

Azimuthal amplitude inversion in stress-induced anisotropic media based on stress-dependence of microcrack compliance

Liang-Yi Deng [a,b,c], Xing-Yao Yin [a,b,c,*], Kun Li [a,b,c], Zheng-Qian Ma [a,b,c], Ya-Ming Yang [a,b,c]

[a] State Key Laboratory of Deep Oil and Gas, China University of Petroleum (East China), Qingdao, 266580, Shandong, China
[b] School of Geosciences, China University of Petroleum (East China), Qingdao, 266580, Shandong, China
[c] Laoshan Laboratory, Qingdao, 266580, Shandong, China

ARTICLE INFO

Article history:
Received 18 February 2025
Received in revised form
27 June 2025
Accepted 9 October 2025
Available online 13 October 2025

Edited by Meng-Jiao Zhou

Keywords:
Stress-induced anisotropy
Microcrack compliance
PP-wave reflection coefficient
Azimuthal amplitude inversion

ABSTRACT

The elastic properties of subsurface rocks are almost always stress-dependent, which is usually attributed to stress-sensitive microcracks. Incorporating the effect of stress on microcrack compliance, we use a novel PP-wave reflection coefficient to implement azimuthal amplitude inversion in an anisotropic media induced by horizontal uniaxial stress. Firstly, we assume the initial unstressed media is elastic and isotropic, and possesses a dual-porosity system with stress-insensitive background and randomly distributed and randomly orientated microcracks. When such the media is subjected to horizontal uniaxial stress, normal and tangential compliances of microcracks decrease depending on their orientation with respect to the applied stress. A corresponding stress-induced anisotropy model is proposed, and then utilized to construct the effective elastic stiffness tensor of the uniaxial-stress-induced anisotropic media under the assumption of weak anisotropy. Two stress-induced anisotropy parameters (SIAPs), defined as the combination of elastic modulus, microcrack normal/tangential compliance and horizontal uniaxial stress, are introduced to quantify the magnitude of stress-induced normal and tangential anisotropy, respectively. Existing laboratory data of an uniaxially stressed rock sample illustrate that the effective elastic stiffness tensor possesses satisfactory accuracy. Subsequently, combining the perturbation of the stiffness tensor and the scattering theory, a linearized PP-wave reflection coefficient is established in terms of P-wave modulus, shear modulus, density and SIAPs. The effect of stress on seismic response characteristics is thoroughly analyzed. Finally, based on the azimuthal amplitude difference inversion method with the Cauchy-sparse and low-frequency prior regularization, the SIAPs are estimated form azimuthal seismic data. The inverted SIAPs are then used as inputs to estimate the remaining isotropic parameters. Numerical experiments and field data are used to illustrate the feasibility of the inversion method.

1. Introduction

Seismic anisotropy is omnipresent in the Earth's interior, which reveals that the seismic wave velocity, amplitude, and other physical properties vary with direction. The physical mechanisms that cause anisotropy are diverse, including preferentially oriented crystals or minerals, fine layering or alignment of clay particles, stacking of layers with varying elastic properties, oriented fractures, and in-situ stress (Thomsen, 1986; Maupin et al., 2007; Liu and Martinez, 2014). As one of the main sources of seismic anisotropy, in-situ stress is often ignored when carrying out seismic anisotropy research. However, the horizontal in-situ stress, mainly caused by engineering production, tectonic movement and natural chemical reaction, is widespread in subsurface Earth (Sheikholeslami et al., 2021). In some regions, seismic anisotropy has been proven to be consistent with the maximum horizontal compressive stress (S_{Hmax}) (Boness and Zoback, 2006; Pastori et al., 2009; Aiman et al., 2023). Consequently, incorporating the influence of stress on rock properties into seismic anisotropy has crucial practical applications in reservoir detection (Zong et al., 2015), in-situ stress estimation (Aiman et al., 2023; Cao et al., 2025) and hydrocarbon exploration (Wang et al., 2022; Ma et al., 2022).

The elastic properties of crustal rocks are almost always stress-dependent. Many experiments have demonstrated that the

* Corresponding author.
E-mail address: xyyin@upc.edu.cn (X.-Y. Yin).
Peer review under the responsibility of China University of Petroleum (Beijing).

https://doi.org/10.1016/j.petsci.2025.10.002

application of uniaxial stress to a rock induces elastic anisotropy (Nur and Simmons, 1969; Mavko et al., 1995; Sarkar et al., 2003). Theoretically, stress-induced anisotropy model can quantitatively reveal the interaction between in-situ stress and the corresponding induced anisotropy. Third-order elasticity (TOE) theory, also known as acoustoelasticity theory, is widely applied to describe the stress-dependence of rock properties. Johnson and Rasolofosaon (1996) successfully used the TOE theory to characterize the phenomenon that an initially isotropic media subjected to uniaxial stress becomes a transverse isotropic (TI) media. Under the assumption of weak background and stress-induced anisotropy, Sarkar et al. (2003) demonstrated that an isotropic solid in the presence of uniaxial stress exhibits symmetry close to hexagonal. Although TOE theory has a superior ability of representing a complete framework that can compute signatures between arbitrary stress field and the corresponding anisotropic stiffness tenor, it ignores the effect of stress on the rock microstructure. In fact, the stress-dependent rock properties can be explained as the response of internal discontinuities, such as compliant grain contacts and microcracks, to the applied stress (Nur and Simmons, 1969; Mavko et al., 1995; Sayers and Kachanov, 1995; Angus et al., 2009; Sayers et al., 2024). In this study, we use the word "microcrack" to describe the stress-sensitive discontinuity, which displays a multitude of different orientations. If anisotropic stress is applied, microcracks will undergo anisotropic changes, resulting in elastic anisotropy of the rock. Shapiro and Kaselow (2005) described the stress-dependence of the elastic moduli of rocks by investigating the effect of stress as a result of pore space deformation. Considering the exponential dependence of the area of the displacement microcracks, analytical models have been proposed to describe uniaxial-stress-induced anisotropy (Gurevich et al., 2011). Compared to their studies, we explore the stress-dependence of rock properties through microcrack compliance, a crucial ingredient for assessing rock stiffness and strength (Griffiths et al., 2017; Sayers et al., 2024). When an elastic isotropic media is subjected to horizontal uniaxial load, the effect of preferential decrease of microcrack compliance is emphasized and a corresponding stress-induced anisotropy model is proposed.

The PP-wave reflection coefficient, serving as a critical link between the observed seismic data and the elastic, anisotropic or petrophysical parameters, can provide valuable information for amplitude variation with offset/angle and azimuth (AVOA/AVAZ). Many scholars have made landmark contributions in deriving the reflection coefficients at an interface between two distinct media, including isotropic media (Aki and Richards, 1980), fracture-induced anisotropic media (Far et al., 2013; Rüger, 1997), and even arbitrary anisotropic media (Pšenčík and Martins, 2001; Shaw and Sen, 2006). On this basis, the TOE theory is used to consider the effect of stress. Taking the initial stress into consideration, Sharma (2007) studied the propagation of plane waves in a generally anisotropic elastic media. Liu et al. (2012) discussed the reflection and transmission of plane wave at the interface between fluid and stressed rock. Chen et al. (2023) proposed the dynamic elastic wave equations for fluid-saturated porous layered media to study the effect of horizontal uniaxial stress-induced anisotropy on shear wave splitting. Li and Hu (2023) investigated the reflection and transmission for the quasi-P-wave incident on the welded and non-welded interfaces between two stressed rocks by using TOE theory. Compared to the complexity of the exact equations, the approximate PP-wave reflection coefficient, expressed as a linear combination of the relevant model parameters, shows superiority in practical applications. Based on the variants of the TOE theory, involving certain modifications such as weak anisotropy assumption or small strain/stress approximation, many linearized stress-dependent PP-wave reflection coefficients have been proposed. By substituting the anisotropic parameters of a rock subjected to uniaxial stress into a well-known approximate PP-wave reflection coefficient in horizontal transversely isotropic (HTI) media (Rüger, 1997), Liu et al. (2009) derived a linear PP-wave reflection coefficient for HTI media induced by uniaxial stress. Based on the TOE theory, the PP-wave reflection coefficients of biaxial stress-induced anisotropic media and overburden-stressed isotropic media have been proposed (Chen and Zong, 2022; Chen et al., 2024). Following nonlinear acoustoelastic theory, the decoupled fracture- and stress-induced PP-wave reflection coefficients in horizontally stressed HTI media and horizontally stressed vertical transversely isotropic (VTI) media are derived (Pan and Zhao, 2024; Pan et al., 2024). Despite considerable efforts have been made, we have yet to find one incorporating the effect of stress on microcrack compliance, although it can be regarded as the mechanism of stress-induced anisotropy.

Furthermore, azimuthal amplitude inversion is an effective tool for obtaining stratigraphic properties, especially anisotropy information, from azimuthal seismic data (Shaw and Sen, 2006; Far et al., 2013; Pan and Zhao, 2024). Unfortunately, the contribution of anisotropic parameters to the reflection coefficient is much smaller than that of isotropic parameters, which makes it difficult to simultaneously invert multi-parameters based on the linear approximation of the reflection equation for anisotropic media. To improve the stability and accuracy of anisotropic seismic inversion, many strategies have been proposed, such as the azimuthal Fourier series expansion method (Ma et al., 2022), the parameter combination method (Zong and Ji, 2021), and the azimuthal amplitude difference inversion method (Chen et al., 2017). However, deriving the Fourier series of a reflection coefficient requires extensive mathematical calculations. And model parameterization relies on strict assumptions during derivation, and the inversion result is a combination of parameter attributes. In contrast, the azimuthal amplitude difference inversion method can leverage the azimuthal difference of reflection coefficient to invert anisotropic parameters. Subsequently, the inverted anisotropic parameters can serve as prior information to achieve the estimation of the remaining isotropic parameters. This method is more convenient to operate and provides a stepwise solution for estimating the overall model parameters in azimuthally anisotropic media.

The article is organized as follows. Firstly, considering the stress-dependence of the normal and tangential compliances of microcracks, we derive an analytical model to explain the anisotropy induced by the application of horizontal uniaxial stress to an elastic isotropic media. Furthermore, based on the equivalent medium theory and the assumption of weak anisotropy, the model is employed to construct the effective elastic stiffness tensor of the uniaxial-stress-induced anisotropic media. Then, by perturbing the effective elastic stiffness tensor components and relating the perturbations to the reflection coefficient via Born scattering theory, an approximate PP-wave reflection coefficient is proposed. Seismic response characteristics of this media at different stress levels are analyzed. Finally, we implement a stepwise azimuthal amplitude inversion in the uniaxial-stress-induced anisotropic media. The robustness and suitability of the inversion method is tested with numerical experiments and field data.

2. Characterization of anisotropy induced by horizontal uniaxial stress

Although quite a few researches have been carried out on fracture-induced anisotropy, in-situ stress can affect the rock microstructure, thereby also inducing anisotropy. We assume that the unstressed media is elastic and isotropic, and can be characterized by a dual-porosity system with stress-insensitive

background and stress-sensitive microcracks (Shapiro and Kaselow, 2005; Gurevich et al., 2011; Sayers et al., 2024). Based on the excess compliance theory (Sayers and Kachanov, 1995), the elastic anisotropy and stress-dependence of microcracks can be expressed as an excess compliance tensor, given by

$$\Delta \mathbf{S}_{ijkl} = \frac{1}{4}\left(\boldsymbol{\alpha}_{ik}\delta_{jl} + \boldsymbol{\alpha}_{il}\delta_{jk} + \boldsymbol{\alpha}_{jk}\delta_{il} + \boldsymbol{\alpha}_{jl}\delta_{ik}\right) + \boldsymbol{\beta}_{ijkl} \tag{1}$$

where δ_{ij} is the Kronecker delta. $\boldsymbol{\alpha}_{ij}$ and $\boldsymbol{\beta}_{ijkl}$ are second- and fourth-rank compliance tensors, which are dependent on the number of microcracks, their area and their normal and tangential compliances. In order to quantify the effect of microcracks, we define the position of a certain microcrack by introducing a spherical coordinate system. Then, the components of normal direction $\mathbf{n}$ of the microcrack are

$$n_1 = \sin\theta_p \cdot \cos\theta_a,\ n_2 = \sin\theta_p \cdot \sin\theta_a,\ \text{ and }\ n_3 = \cos\theta_p \tag{2}$$

where θ_p and θ_a are the polar angle and azimuth in the orientation normal to the microcrack, respectively.

Assuming that the microcracks within the unstressed media are identical, rotationally invariant, randomly orientated and randomly distributed, the second- and fourth-rank tensors are continuous functions of angular coordinate. Therefore, the components of the second- and fourth-rank compliance tensors can be analytically calculated using spherical integral (Sayers, 2002; Sayers et al., 2024):

$$\alpha_{ij} = \frac{1}{4\pi}\int_{\theta_p=0}^{\pi}\int_{\theta_a=0}^{2\pi} \Omega_T(\theta_p,\theta_a) n_i n_j \sin\theta_p \mathrm{d}\theta_p \mathrm{d}\theta_a \tag{3}$$

$$\beta_{ijkl} = \frac{1}{4\pi}\int_{\theta_p=0}^{\pi}\int_{\theta_a=0}^{2\pi} \left[\Omega_N(\theta_p,\theta_a) - \Omega_T(\theta_p,\theta_a)\right] n_i n_j n_k n_l \sin\theta_p \mathrm{d}\theta_p \mathrm{d}\theta_a \tag{4}$$

where $\Omega_N(\theta_p,\theta_a)\sin\theta_p \mathrm{d}\theta_p \mathrm{d}\theta_a$ and $\Omega_T(\theta_p,\theta_a)\sin\theta_p \mathrm{d}\theta_p \mathrm{d}\theta_a$ are the normal and tangential compliances of microcracks in the angular range of normal direction from θ_p to $\theta_p + \mathrm{d}\theta_p$ and θ_a to $\theta_a + \mathrm{d}\theta_a$, respectively.

Subsequently, we consider the scenario that the elastic isotropic media is subjected to horizontal uniaxial stress τ_{11} (The model is shown in Fig. 1). Following Mavko et al. (1995), Shapiro and Kaselow (2005) and Sayers et al. (2024), we assume that the normal and tangential compliances of microcracks in a particular direction decay exponentially with the normal compressive stress τ_n acting on that direction, given by

$$\Omega_N = \Omega_{N0}\exp\left(-\frac{\tau_n}{P_{Nc}}\right) \tag{5}$$

$$\Omega_T = \Omega_{T0}\exp\left(-\frac{\tau_n}{P_{Tc}}\right) \tag{6}$$

where Ω_{N0} and Ω_{T0} denote the normal and tangential compliances of microcracks before the application of stress, respectively, $\tau_n = \tau_{11}n_1^2$ is the stress applied in the direction normal to the microcracks, and parameters P_{Nc} and P_{Tc} are the characteristic stresses representing the rate at which the normal and tangential compliances of microcracks decrease with the applied stress, respectively (Mavko et al., 1995; Gurevich et al., 2011; Sayers et al., 2024).

Furthermore, based on the theory of weak anisotropy (Thomsen, 1986), we assume that the applied stress is small enough compared to both P_{Nc} and P_{Tc}, so that the first order Taylor expansion of the exponential function can be used for the exponential decay in Eqs. (5) and (6), given by

$$\Omega_N = \Omega_{N0}\exp\left(-\frac{\tau_{11}}{P_{Nc}}n_1^2\right) \approx \Omega_{N0}\left(1 - \frac{\tau_{11}}{P_{Nc}}n_1^2\right) \tag{7}$$

$$\Omega_T = \Omega_{T0}\exp\left(-\frac{\tau_{11}}{P_{Tc}}n_1^2\right) \approx \Omega_{T0}\left(1 - \frac{\tau_{11}}{P_{Tc}}n_1^2\right) \tag{8}$$

Substituting Eqs. (7) and (8) into Eqs. (3) and (4), and calculating the spherical integral with the software Mathematica, the second- and fourth-rank tensors are obtained, which are shown in Appendix A. Subsequently, substituting them into Eq. (1) and rewriting the excess compliance tensor $\Delta\mathbf{S}_{ijkl}$ in the form of a 6×6 tensor $\Delta\mathbf{S}_{ij}$ using the Voigt notation (Sayers, 2002), the excess compliance tensor of the anisotropic media induced by horizontal uniaxial stress can be computed as (The specific derivation is shown in Appendix A)

$$\Delta\mathbf{S}_{ij} = \Delta\mathbf{S}_{ij}^{iso} + \tau_{11-N}\Delta\mathbf{S}_{ij}^{ani-N} + \tau_{11-T}\Delta\mathbf{S}_{ij}^{ani-T} \tag{9}$$

where $\Delta\mathbf{S}_{ij}^{iso}$ is the excess compliance tensor of the isotropic distribution of microcracks in the unstressed rock, $\Delta\mathbf{S}_{ij}^{ani-N}$ and $\Delta\mathbf{S}_{ij}^{ani-T}$ are the excess compliance tensors due to the effect of horizontal uniaxial stress on the normal and tangential compliances of the microcracks, respectively, and the normalized stresses are given by $\tau_{11-N} = \tau_{11}/P_{Nc}$ and $\tau_{11-T} = \tau_{11}/P_{Tc}$, respectively. To some extent, this model is formally similar to Gurevich et al. (2011), which reflects its plausibility. Meanwhile, the stress-dependence of the normal and tangential compliances of microcracks is considered, providing a new perspective on stress-induced anisotropy.

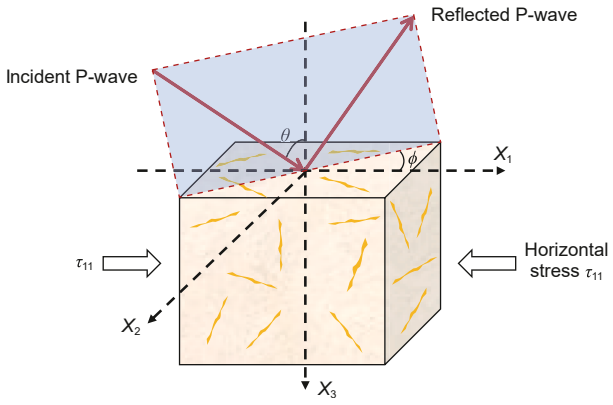

Fig. 1. Schematic illustration of incident P-wave propagation in an elastic isotropic media subjected to horizontal uniaxial stress. The unstressed media possesses a dual-porosity system with stress-insensitive background and randomly distributed and randomly orientated microcracks. θ and ϕ represent the incident angle and observation azimuth, respectively.

3. Parameterization of stiffness tensor in an anisotropic media induced by horizontal uniaxial stress

Combining the excess compliance theory and Eq. (9), the complete compliance tensor $\mathbf{S}_{ij}$ of an anisotropic media induced by horizontal uniaxial stress can be expressed as

$$\mathbf{S}_{ij} = \underbrace{\mathbf{S}_{ij}^{b} + \Delta\mathbf{S}_{ij}^{iso}}_{\mathbf{S}_{ij}^{0}} + \tau_{11-N}\Delta\mathbf{S}_{ij}^{ani-N} + \tau_{11-T}\Delta\mathbf{S}_{ij}^{ani-T} \tag{10}$$

where $\mathbf{S}_{ij}^{b}$ is the compliance tensor of the stress-insensitive background estimated from the mineral composition (Angus et al., 2009) or behavior at high pressures (Sayers, 2002), and $\mathbf{S}_{ij}^{0}$ is the effective compliance tensor of the unstressed media.

According to the non-interactive approximation theory, the effective compliance tensor of a cracked media can be expressed as the sum of the background compliance tensor and the excess compliance tensor of the microcracks (Liu and Martinez, 2014). Therefore, the effective stiffness tensor $\mathbf{C}_{ij}^{0} = \left(\mathbf{S}_{ij}^{0}\right)^{-1}$ of the unstressed media can be computed as

$$\mathbf{C}_{ij}^{0} = \left[\mathbf{S}_{ij}^{b} + \Delta\mathbf{S}_{ij}^{iso}\right]^{-1} = \begin{bmatrix} M & \lambda & \lambda & 0 & 0 & 0 \\ \lambda & M & \lambda & 0 & 0 & 0 \\ \lambda & \lambda & M & 0 & 0 & 0 \\ 0 & 0 & 0 & \mu & 0 & 0 \\ 0 & 0 & 0 & 0 & \mu & 0 \\ 0 & 0 & 0 & 0 & 0 & \mu \end{bmatrix} \tag{11}$$

where $M = \lambda + 2\mu = \rho\alpha^2$, and M, λ, μ, ρ and α denote P-wave modulus, the first Lamé constant, shear modulus, background density, seismic P-wave velocity of the unstressed media, respectively.

To validate the randomly distributed and randomly oriented microcrack model, we assume that the microcracks are penny-shaped. Then, Ω_{N0} and Ω_{T0} can be expressed as follows (Li et al., 2023):

$$\Omega_{N0} = \frac{4(\lambda_0 + 2\mu_0)}{3\mu_0(\lambda_0 + \mu_0)} e \tag{12}$$

$$\Omega_{T0} = \frac{16(\lambda_0 + 2\mu_0)}{3\mu_0(3\lambda_0 + 4\mu_0)} e \tag{13}$$

where λ_0 and μ_0 denote the Lamé constants of the stress-insensitive background, and e is the density of the microcracks (Hudson, 1981).

Combining Eqs. (11)–(13) and Eq. (A-5), to calculate the effective P-wave modulus and shear modulus and compare them with the Kuster-Toksöz (K-T) model (Kuster and Toksöz, 1974), as shown in Fig. 2. Besides, to ensure the rationality of the model, we choose a stiff background sample with P-wave and shear modulus of 33.992 GPa and 13.225 GPa, respectively, and a soft background sample with P-wave and shear modulus of 14.160 GPa and 5.687 GPa, respectively. From Fig. 2(a) and (b), it can be seen that for both stiff and soft samples, the results of our model and K-T model are in good agreement.

Subsequently, when the isotropic elastic rock is subjected to horizontal uniaxial stress τ_{11}, anisotropy is induced due to the preferential decrease of microcrack compliance, as shown in Eq. (9). Under the assumption of weak anisotropy, the stress-induced normal and tangential anisotropy is weak enough compared to the unstressed media. Therefore, the stiffness tensor $\mathbf{C}_{ij}$ of the anisotropic media induced by horizontal uniaxial stress can be derived as (Bakulin et al., 2000; Chen et al., 2017; Pan et al., 2024)

$$\begin{aligned} \mathbf{C}_{ij} &= \mathbf{C}_{ij}^{0} - \tau_{11-N}\mathbf{C}_{ij}^{0}\Delta\mathbf{S}_{ij}^{ani-N}\mathbf{C}_{ij}^{0} - \tau_{11-T}\mathbf{C}_{ij}^{0}\Delta\mathbf{S}_{ij}^{ani-T}\mathbf{C}_{ij}^{0} \\ &= \begin{bmatrix} C_{11} & C_{12} & C_{12} & 0 & 0 & 0 \\ C_{12} & C_{22} & C_{22}-2C_{44} & 0 & 0 & 0 \\ C_{12} & C_{22}-2C_{44} & C_{22} & 0 & 0 & 0 \\ 0 & 0 & 0 & C_{44} & 0 & 0 \\ 0 & 0 & 0 & 0 & C_{55} & 0 \\ 0 & 0 & 0 & 0 & 0 & C_{55} \end{bmatrix} \end{aligned} \tag{14}$$

where

$$\begin{aligned} C_{11} = M &- \left(\frac{8}{105}\lambda^2 + \frac{4}{35}M\lambda + \frac{1}{7}M^2\right)\tau_{11-N}\Omega_{N0} \\ &- \left(\frac{2}{35}\lambda^2 - \frac{4}{35}M\lambda + \frac{2}{35}M^2\right)\tau_{11-T}\Omega_{T0} \end{aligned} \tag{15}$$

$$\begin{aligned} C_{12} = \lambda &- \left(\frac{2}{21}\lambda^2 + \frac{22}{105}M\lambda + \frac{1}{35}M^2\right)\tau_{11-N}\Omega_{N0} \\ &- \left(-\frac{1}{35}\lambda^2 + \frac{2}{35}M\lambda - \frac{1}{35}M^2\right)\tau_{11-T}\Omega_{T0} \end{aligned} \tag{16}$$

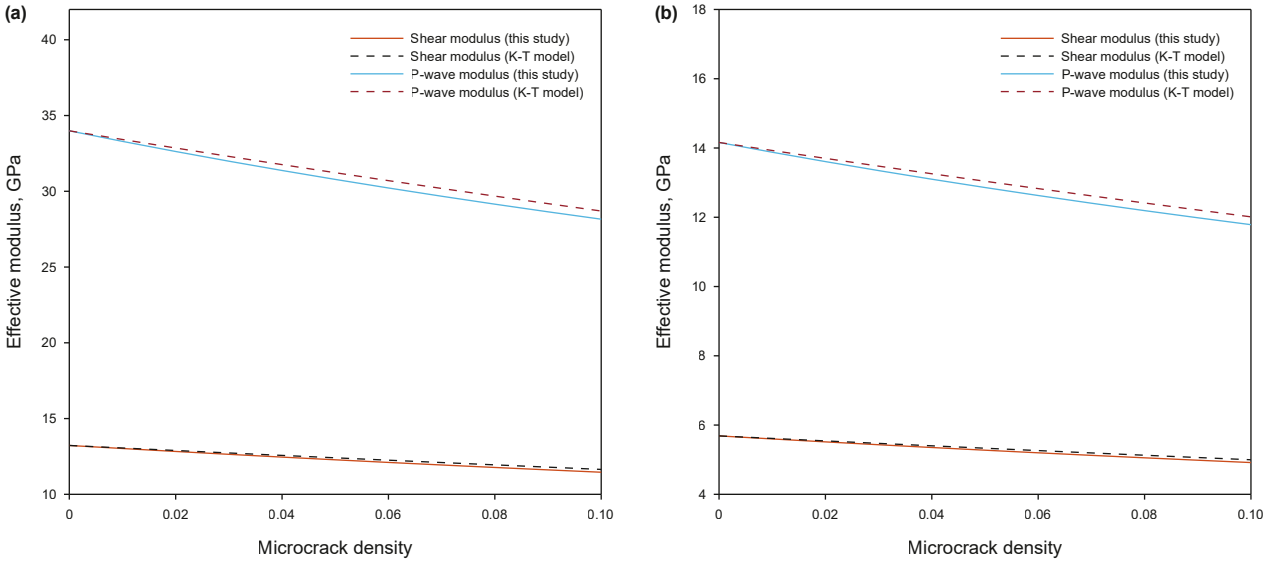

Fig. 2. Variations in effective elastic properties with microcrack density for rocks permeated by randomly distributed and randomly oriented microcracks: **(a)** results for a stiff sample, **(b)** results for a soft sample. The dashed and solid lines are calculated using the K-T model and our model, respectively.

Table 1
Elastic properties of rock samples.

Rock elastic parameters	Rock samples				
	Nur and Simmons (1969)	Chaudhry (1995)	Han et al. (1986)		
	Barre granite	Penrith sandstone	Mexico A sandstone	Mexico B sandstone	Mexico C sandstone
M, GPa	38.2	25.5	16.5	17.2	29.9
μ, GPa	18.3	10.8	6.6	6.6	11.6
ρ, g/cm^3	2.66	2.77	1.78	1.79	2.08
Ω_{N0}, GPa^{-1}	0.0422	0.0413	0.0212	0.0273	0.0216
Ω_{T0}, GPa^{-1}	0.024	0.086	0.0333	0.0379	0.0267
$P_{Nc} = P_{Tc}$, MPa	18.3	13.4	7.8	8.3	10.9

$$C_{22} = M - \left(\frac{8}{35}\lambda^2 + \frac{8}{105}M\lambda + \frac{1}{35}M^2\right)\tau_{11-N}\Omega_{N0} - \left(\frac{4}{105}\lambda^2 - \frac{8}{105}M\lambda + \frac{4}{105}M^2\right)\tau_{11-T}\Omega_{T0} \tag{17}$$

$$C_{44} = \mu - \frac{4}{105}\mu^2\tau_{11-N}\Omega_{N0} - \frac{2}{21}\mu^2\tau_{11-T}\Omega_{T0} \tag{18}$$

$$C_{55} = \mu - \frac{4}{35}\mu^2\tau_{11-N}\Omega_{N0} - \frac{16}{105}\mu^2\tau_{11-T}\Omega_{T0} \tag{19}$$

From the symmetry of the stiffness tensor, we can find that the anisotropic media induced by horizontal uniaxial stress is similar with that of an unstressed transversely isotropic media with a horizontal symmetry axis (i.e., HTI media). In order to simplify Eqs. (15)–(19), we define

$$\Psi_N = -\tau_{11-N}M\Omega_{N0} \tag{20}$$

$$\Psi_T = -\tau_{11-T}\mu\Omega_{T0} \tag{21}$$

as two stress-induced anisotropy parameters (SIAPs) to represent the stress-induced normal and tangential anisotropy, respectively. Substituting Eqs. (20) and (21) into Eqs. (15)–(19), the elements of the elastic stiffness tensor for the horizontal uniaxial stress-induced anisotropic media can be obtained, which are given in Appendix B.

In order to verify the reasonability and precision of the derived elastic stiffness tensor, we use the laboratory data of Nur and Simmons (1969) on a sample of Barre Granite, which was used previously to test the modelling approach of Mavko et al. (1995) and Gurevich et al. (2011). The velocity variations of the uniaxially stressed rock sample are predicted at different stress levels and compared with the measured velocities. The elastic parameters (M, μ, Ω_{N0}, Ω_{T0}, P_{Nc} and P_{Tc}) of the unstressed rock are determined from a hydrostatic pressure test by the fitting procedure described in Angus et al. (2009) and Gurevich et al. (2011). The fitted elastic parameters of the rock sample are shown in Table 1 and the corresponding P- and SH-wave velocities measured along and perpendicular to the stress direction at different uniaxial stress levels are shown in Table 2. Fig. 3 compares the predicted and measured P- and SH-wave velocities, along and perpendicular to stress direction, versus uniaxial stress. It can be observed that the predictions are consistent with the trend of the laboratory data, verifying the feasibility of the proposed stress-induced anisotropy model. Meanwhile, although stress-induced microcrack closure leads to an overall increase in mechanical stiffness, the increase is greatest along the direction of stress and least in the direction perpendicular to stress. This indicates that stress induces elliptical anisotropy (Johnson and Rasolofosaon, 1996; Gurevich et al., 2011; Sayers et al., 2024).

Table 2
The measured P- and SH-wave velocities of Barre Granite under different uniaxial stresses (Nur and Simmons, 1969). Degrees shown represent angles between the uniaxial stress and the direction of wave propagation.

Stress, MPa	P-wave velocity, m/s		SH-wave velocity, m/s	
	0°	90°	0°	90°
0	3790	3790	2630	2630
5	4040	–	2690	2650
10	4220	3850	2740	2680
15	4370	–	2830	2710
20	4510	3950	2880	2740
25	4600	–	2920	2770
30	4670	4020	2960	2790

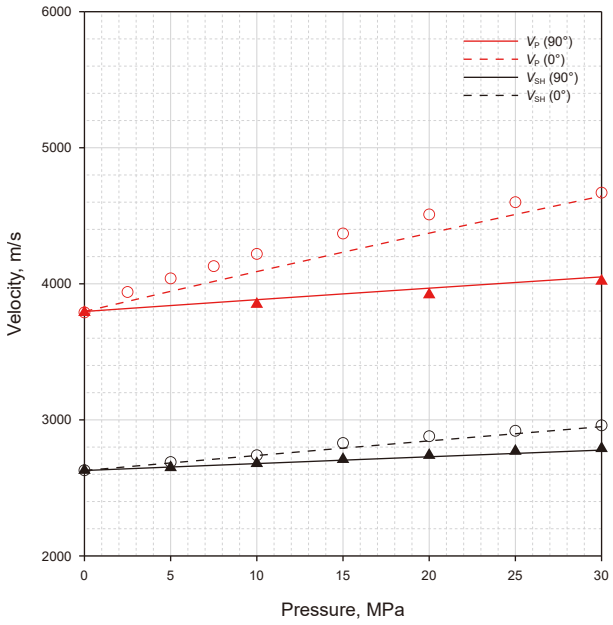

Fig. 3. Measured velocities of P-wave (open symbols) and SH-wave (solid symbols) and model predictions (lines) for a sample of Barre Granite. The dashed and solid lines are predictions of the stress-induced anisotropy model, and the circles and triangles denote the corresponding measurements of Nur and Simmons (1969). The degrees shown represent angles between uniaxial stress and direction of wave propagation.

Based on the method above, we further propose a rock physics modelling process for stress-induced anisotropic media, which lays the groundwork for subsequent seismic inversion. Fig. 4 demonstrates the detailed rock physics modelling process. The stress-insensitive background can be constructed by rock minerals, volume fraction and porosity of matrix pores (Hill, 1952; Hornby et al., 1994). Then, the randomly distributed and randomly oriented microcracks are added to obtain the unstressed rock by Eq. (11), and the effect of horizontal uniaxial stress is considered by Eq. (14). The fluid is mixed by the Wood's formula (Wood, 1955) and added through the Brown-Korringa formula (Brown and Korringa, 1975).

4. Linearized PP-wave reflection coefficient

The linearized PP-wave reflection coefficient provides a mathematically tractable approximation for calculating the amplitude of the reflected P-wave. For a stress-induced anisotropic media, both the magnitude and direction of the stress have a dramatic effect on the resulting anisotropy. Moreover, excessive stress can cause the damage or failure of the rock. In the case of an interface separating two distinct uniaxial-stress-induced anisotropic media, the perturbed stiffness tensor is

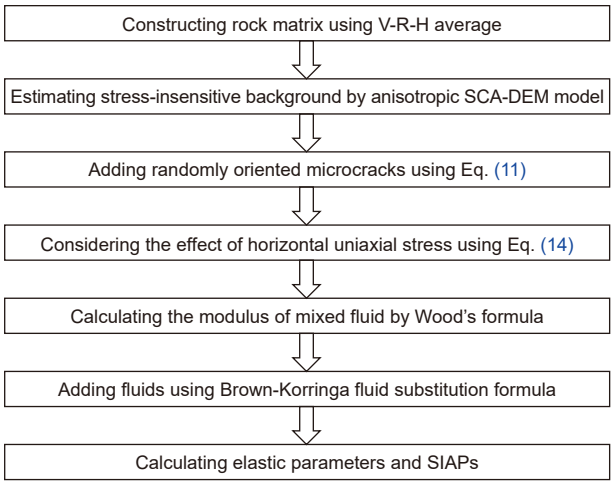

Fig. 4. Flowchart of rock physics modelling of an anisotropic media induced by horizontal uniaxial stress.

$$\Delta\mathbf{C}_{ij}=\begin{bmatrix} \Delta C_{11} & \Delta C_{12} & \Delta C_{12} & 0 & 0 & 0 \\ \Delta C_{12} & \Delta C_{22} & \Delta C_{22}-2\Delta C_{44} & 0 & 0 & 0 \\ \Delta C_{12} & \Delta C_{22}-2\Delta C_{44} & \Delta C_{22} & 0 & 0 & 0 \\ 0 & 0 & 0 & \Delta C_{44} & 0 & 0 \\ 0 & 0 & 0 & 0 & \Delta C_{55} & 0 \\ 0 & 0 & 0 & 0 & 0 & \Delta C_{55} \end{bmatrix} \tag{22}$$

where the detailed expression of $\Delta\mathbf{C}_{ij}$ is given in Appendix B.

Based on the asymptotic ray theory and stationary phase method, Shaw and Sen (2006) derived the relationship between the spatial perturbation of the elastic stiffness tensor and the PP-wave reflection coefficient in an inhomogeneous media, given by

$$R_{\mathrm{PP}}=\frac{1}{4\rho\cos^2\theta}S_{\mathrm{PP}} \tag{23}$$

where θ is the incident angle of the P-wave, and the scattering function S_{PP} is

Table 3
Rock parameters of the two-layer model.

Model	M, GPa	μ, GPa	ρ, g/cm^3	Ω_{N0}, GPa^{-1}	Ω_{T0}, GPa^{-1}	$\tau_{11\text{-N}}=\tau_{11\text{-T}}$
Upper	17.2	7.6	2.21	0.0212	0.0379	0
Lower	20.3	8.45	2.3	0.0345	0.0498	−0.7

Table 4
Procedures of seismic data processing.

1. Data reading and editing
2. Data format transformation
3. Trace editing and regulation
4. Static correction
5. Preserved-amplitude pre-stack processing
6. Deconvolution
7. First break picking and muting
8. Sort common mid-point (CMP) gathers
9. Velocity analysis
10. NMO (normal moveout)
11. DMO (dip moveout)
12. Pre-stack time migration
13. Random noise attenuation
14. Inverse NMO
15. New velocity picking
16. NMO with new velocities
17. Transform to time-angle domain

$$S_{\mathrm{PP}}=\Delta\rho\xi^{\mathrm{PP}}+\sum_{m=1}^{6}\sum_{n=1}^{6}\Delta C_{mn}\eta_{mn}^{\mathrm{PP}} \tag{24}$$

where $\Delta\rho$ is the perturbation in density term, and the Voigt subscripts $m=i\delta_{ij}+(9-i-j)\left(1-\delta_{ij}\right)$, $n=k\delta_{kl}+(9-k-l)(1-\delta_{kl})$. $\xi^{\mathrm{PP}}=\left[\mathbf{g}_i'^{\mathrm{PP}}\mathbf{g}_k^{\mathrm{PP}}\right]\Big|_{\mathbf{r}=\mathbf{r}_0'}$, $\eta_{mn}^{\mathrm{PP}}=\left[\mathbf{p}_j'^{\mathrm{PP}}\mathbf{g}_i'^{\mathrm{PP}}\mathbf{p}_l^{\mathrm{PP}}\mathbf{g}_k^{\mathrm{PP}}\right]\Big|_{\mathbf{r}=\mathbf{r}_0'}$; $\mathbf{p}$ and $\mathbf{g}$ are the slowness and polarization vectors of the incident P-wave; $\mathbf{p}'$ and $\mathbf{g}'$ are slowness and polarization vectors of the reflected P-wave. More expressions of S_{PP} are shown in Appendix C.

According to the equations above, the linearized PP-wave reflection coefficient for the uniaxial-stress-induced anisotropic media can be derived as (The detailed derivation is given in Appendix C)

$$R_{\mathrm{PP}}(\theta,\phi)=R_{\mathrm{PP}}^{\mathrm{iso}}(\theta)+R_{\mathrm{PP}}^{\mathrm{ani-N}}(\theta,\phi)+R_{\mathrm{PP}}^{\mathrm{ani-T}}(\theta,\phi) \tag{25}$$

where

$$R_{\mathrm{PP}}^{\mathrm{iso}}(\theta)=a_M(\theta)\frac{\Delta M}{M}+a_\mu(\theta)\frac{\Delta\mu}{\mu}+a_\rho(\theta)\frac{\Delta\rho}{\rho} \tag{26}$$

$$R_{\mathrm{PP}}^{\mathrm{ani-N}}(\theta,\phi)=a_{\Psi_{\mathrm{N}}}(\theta,\phi)\Delta\Psi_{\mathrm{N}} \tag{27}$$

$$R_{\mathrm{PP}}^{\mathrm{ani-T}}(\theta,\phi)=a_{\Psi_{\mathrm{T}}}(\theta,\phi)\Delta\Psi_{\mathrm{T}} \tag{28}$$

in which

$$a_M(\theta)=\frac{1}{4}\sec^2\theta \tag{29}$$

$$a_\mu(\theta)=-2g\sin^2\theta \tag{30}$$

$$a_\rho(\theta)=\frac{1}{2}\left(1-\frac{\sec^2\theta}{2}\right) \tag{31}$$

$$a_{\Psi_{\mathrm{N}}}(\theta,\phi)=\frac{1}{105}\left[\begin{array}{l}\left(16g^2\sin^2\theta+16g^2\tan^2\theta-14g\tan^2\theta\right)\sin^2\phi+ \\ 24g^2\cos^2\theta+8g^2\tan^2\theta+\left(\frac{35}{4}-14g\right)\sec^2\theta-14g\end{array}\right] \tag{32}$$

$$a_{\Psi_{\mathrm{T}}}(\theta,\phi)=\frac{2g}{105}\left[\left(\tan^2\theta\sin^2\theta-5\sin^2\theta\right)\cos^2\phi-10\sin^2\theta+2\sec^2\theta\right] \tag{33}$$

where ϕ denotes the azimuthal phase angle ($\phi=0^\circ$ for the direction along the applied horizontal uniaxial stress) and the denominators of $\Delta M/M$, $\Delta\mu/\mu$, $\Delta\rho/\rho$ represent the average values of the parameters of the upper medium and the lower medium at the interface.

It is worth mentioning that the novel PP-wave reflection coefficient of the anisotropic media induced by uniaxial stress can be divided into three parts: $R_{\mathrm{PP}}^{\mathrm{iso}}(\theta)$ represents the reflection coefficients in the absence of stress, $R_{\mathrm{PP}}^{\mathrm{ani-N}}(\theta,\phi)$ and $R_{\mathrm{PP}}^{\mathrm{ani-T}}(\theta,\phi)$ represent the normal and tangential anisotropic perturbations of these coefficients for the weakly anisotropic media induced by horizontal uniaxial stress (Shaw and Sen, 2006).

To illustrate the newly derived PP-wave refection coefficient, we design a two-layer model with weak property contrasts, and the model parameters are shown in Table 3. Subsequently, the novel reflection coefficient of Eq. (25) is calculated and compared

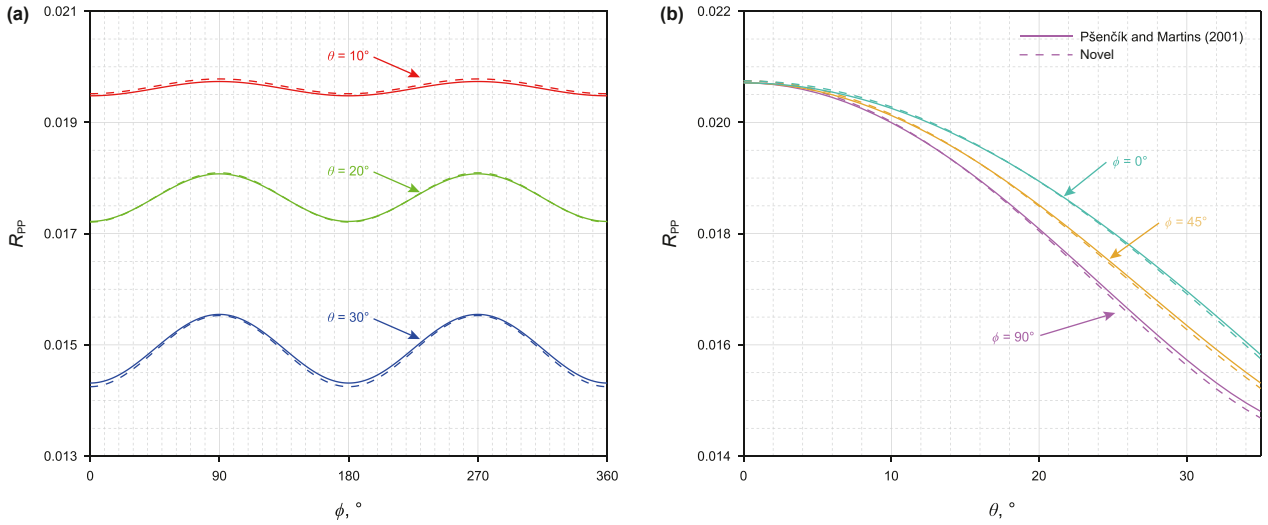

Fig. 5. Comparisons of the novel reflection coefficient (the dashed lines) with the Pšenčík and Martins (2001) approximate formula (the solid lines). The variation of PP-wave reflection coefficient with **(a)** azimuth and **(b)** incident angle, respectively.

with the formula of Pšenčík and Martins (2001). Fig. 5(a) demonstrates the variation of PP-wave reflection coefficients with azimuth for incident angles of 10°, 20° and 30°. Fig. 5(b) demonstrates the variation of PP-wave reflection coefficient with incident angle for azimuths of 0°, 45°, and 90°. It can be seen that the derived reflection coefficient shows a high degree of conformance with the formula of Pšenčík and Martins (2001). Therefore, we conclude that the accuracy of the novel PP-wave reflection coefficient for the anisotropic media induced by horizontal uniaxial stress can meet the requirements of subsequent seismic inversion.

5. Azimuthal amplitude inversion

5.1. Contribution analysis of model parameters

The accuracies of the inversion results depend on the contribution of model parameters on the reflection coefficient, as shown in Fig. 6. Fig. 6(a)–(c) represent that background elastic parameters (M, μ and ρ) remain unaffected by azimuthal variations, while the reflection coefficient increases with higher values of $\Delta M/M$ and $\Delta\rho/\rho$, and decreases as $\Delta\mu/\mu$ rises. Fig. 6(d) and (e) represent that the SIAPs can contribute to the reflection amplitude variations with the incident angle and azimuth (AVAZ), and the effect of perturbations in stress-induced tangential anisotropy parameter Ψ_T is larger than that of stress-induced normal anisotropy parameter Ψ_N. This may be explained that the normal compliance Ω_N decreases faster with increasing compressive stress than the tangential compliance Ω_T (Sayers et al., 2024). A comparison between Fig. 6(a)–(c) with Fig. 6(d) and (e) indicates that the contributions of SIAPs to the reflection coefficient are much lower than that of the isotropic parameters, posing challenges for the multi-parameter simultaneous inversion. Therefore, the azimuthal amplitude difference inversion emerges as the preferred methodology. Moreover, Fig. 6(d) and (e) reveal that reflection amplitude difference is most pronounced between the stress direction $\phi_0 = 0°$ and the direction perpendicular to the stress direction $\phi_\perp = 90°$. This provides favorable priori knowledge for azimuth selection in stress-induced anisotropy inversion.

As shown in Fig. 7, a stepwise azimuthal amplitude inversion strategy is adopted to estimate the model parameters in stress-induced anisotropic media. We firstly apply azimuthal seismic amplitude difference inversion to estimate SIAPs through the seismic data with azimuth ϕ_0 and azimuth $\phi_\perp$. In the second step, the inverted SIAPs are used as inputs to remove the effect of stress on observed seismic data. Then, the background isotropic parameters can be estimated through AVA inversion.

5.2. First step: azimuthal amplitude difference inversion for SIAPs

Based on Eq. (25), the difference of PP-wave reflection coefficient between azimuths ϕ_0 and $\phi_\perp$ is

$$\Delta R_{PP}(\theta,\Delta\phi) = R_{PP}(\theta,\phi_0) - R_{PP}(\theta,\phi_\perp) = a_{\Psi_N}(\theta,\Delta\phi)\Delta\Psi_N + a_{\Psi_T}(\theta,\Delta\phi)\Delta\Psi_T \tag{34}$$

where

$$a_{\Psi_N}(\theta,\Delta\phi) = a_{\Psi_N}(\theta,\phi_0) - a_{\Psi_N}(\theta,\phi_\perp) \tag{35}$$

$$a_{\Psi_T}(\theta,\Delta\phi) = a_{\Psi_T}(\theta,\phi_0) - a_{\Psi_T}(\theta,\phi_\perp) \tag{36}$$

Combining the convolution model and Eq. (34), the azimuthal seismic amplitude difference can be formulated in the matrix form as

$$\mathbf{d} = \mathbf{GX} \tag{37}$$

where

$$\mathbf{G} = \begin{bmatrix} a_{\Psi_N}(\theta_1,\Delta\phi)\mathbf{W}(\theta_1,\Delta\phi)\mathbf{L} & a_{\Psi_T}(\theta_1,\Delta\phi)\mathbf{W}(\theta_1,\Delta\phi)\mathbf{L} \\ a_{\Psi_N}(\theta_2,\Delta\phi)\mathbf{W}(\theta_2,\Delta\phi)\mathbf{L} & a_{\Psi_T}(\theta_2,\Delta\phi)\mathbf{W}(\theta_1,\Delta\phi)\mathbf{L} \\ \vdots & \vdots \\ a_{\Psi_N}(\theta_h,\Delta\phi)\mathbf{W}(\theta_h,\Delta\phi)\mathbf{L} & a_{\Psi_T}(\theta_h,\Delta\phi)\mathbf{W}(\theta_h,\Delta\phi)\mathbf{L} \end{bmatrix}$$

$$\mathbf{d} = \left[\mathbf{d}(\theta_1,\Delta\phi),\quad \mathbf{d}(\theta_2,\Delta\phi),\quad \cdots\quad \mathbf{d}(\theta_h,\Delta\phi)\right]^T, \mathbf{X} = \left[\Psi_N \quad \Psi_T\right]^T \tag{38}$$

and $\mathbf{d}(\theta_i, \Delta\phi)$ is the amplitude difference seismic data with incident angle θ_i ($i = 1, 2, \ldots, h$) and azimuths of ϕ_0 and $\phi_\perp$; $\mathbf{W}$ is the incident angle and azimuth-dependent seismic wavelet; $\mathbf{L}$ is the first-order difference operator; $\mathbf{X}$ is the anisotropic parameter to be inverted and consists of Ψ_N and Ψ_T; and $\mathbf{G}$ is the forward operator with respect to Ψ_N and Ψ_T.

According to the least square criterion, the misfit between the observed seismic data and the synthetic seismic data is measured by the L_2 norm. And the loss function is constructed as follows:

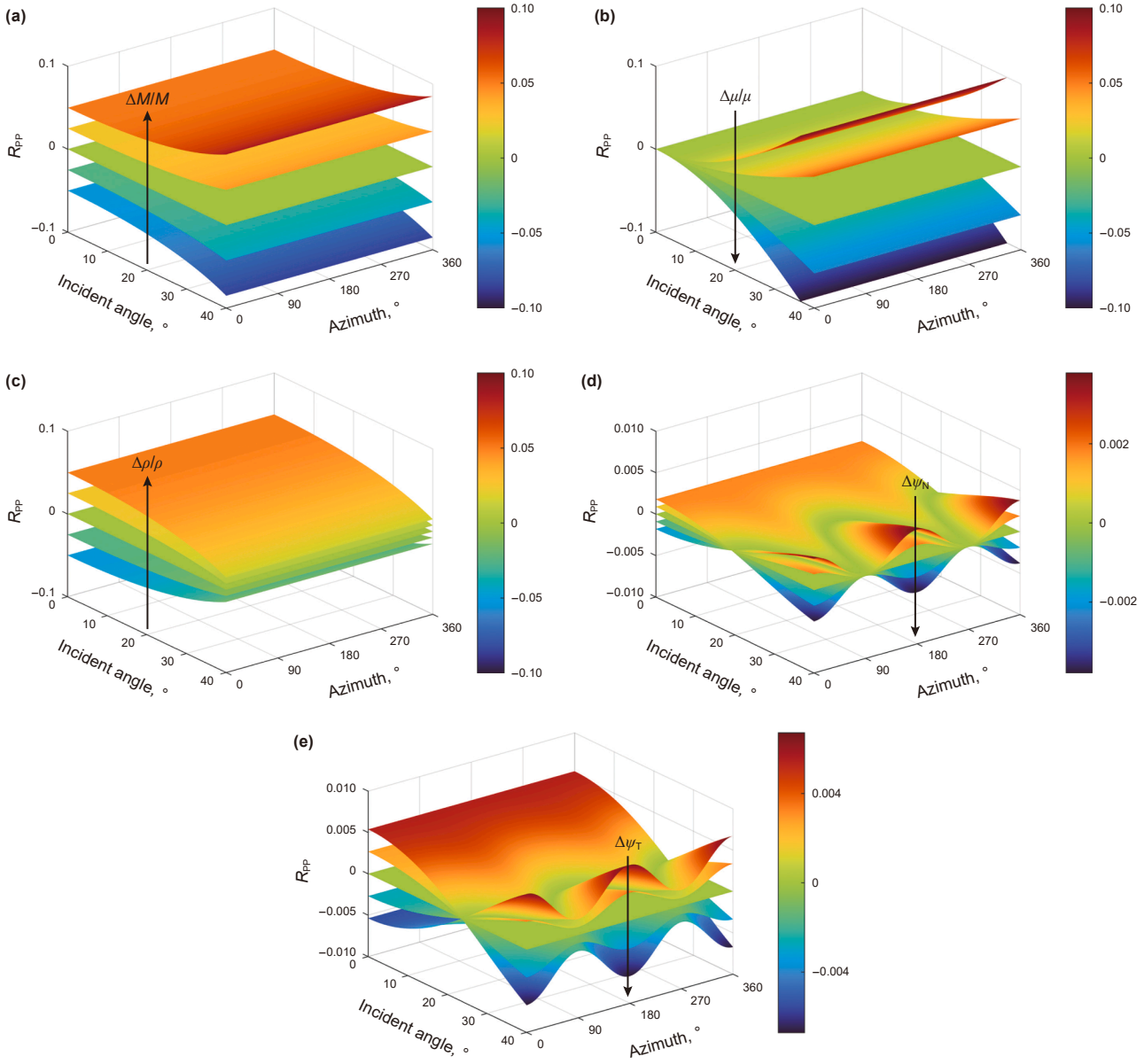

Fig. 6. The effect of model parameters on the reflection coefficient: **(a)** $\Delta M/M$, **(b)** $\Delta\mu/\mu$, **(c)** $\Delta\rho/\rho$, **(d)** $\Delta\Psi_N$ and **(e)** $\Delta\Psi_T$. Each parameter ranges from −0.2 to 0.2 in step of 0.1, and the arrow indicates the direction in which the parameter increases.

$$J_{\text{loss}}(\mathbf{X}) = \min_{\mathbf{X}}\left\{\|\mathbf{d} - \mathbf{G}\mathbf{X}\|_2^2\right\} \tag{39}$$

To improve the resolution to solve Eq. (39), the Cauchy-sparse regularization (Zong et al., 2015; Chen et al., 2017; Wang et al., 2020; Pan and Zhao, 2024) is applied. In addition, the low-frequency models can compensate for relatively weak and noise-susceptible low-frequency components, thereby improving the stability and reliability of the inversion results (Li et al., 2020). Therefore, the objective function of the first-step inversion can be established as

$$\begin{aligned} J_1(\mathbf{X}) &= J_{\text{loss}}(\mathbf{X}) + J_{\text{Cauchy}}(\mathbf{X}) + J_{\text{low}}(\mathbf{X}) \\ &= \min_{\mathbf{X}}\left\{\|\mathbf{d} - \mathbf{G}\mathbf{X}\|_2^2 + \eta\sum_{i=1}^{2}\ln\left(1 + \mathbf{X}_i^2/\sigma_{\mathbf{X}}^2\right) + \sum_{i=1}^{2} r_i\|\zeta_i - \mathbf{Q}_i\mathbf{X}_i\|_2^2\right\} \end{aligned} \tag{40}$$

where

$$\zeta_i = \frac{1}{2}\ln\left(\frac{\mathbf{X}_i}{\mathbf{X}_{i0}}\right), \quad \mathbf{Q} = \int_{t_0}^{t_i} \mathrm{d}\tau \tag{41}$$

and $\eta = \sigma_n^2$ denotes the Cauchy-sparse regularization coefficient; σ_n^2 and $\sigma_{\mathbf{X}}^2$ denote the variances of noise and unknown parameters, respectively; r_i $(i = 1, 2)$ are constraint factors of two model parameters; $\mathbf{X}_{i0}$ is the initial value of the relevant model parameter, which can be estimated from logging curves.

The optimal solutions for model parameters can be obtained by taking the gradient of $\mathbf{X}$ through Eq. (40), given by

$$\left[\mathbf{G}^{\mathrm{T}}\mathbf{G} + \sum_{i=1}^{2} r_i\mathbf{Q}_i^{\mathrm{T}}\mathbf{Q}_i + \eta\mathbf{V}(\mathbf{X})\right]\mathbf{X} = \mathbf{G}^{\mathrm{T}}\mathbf{d} + \sum_{i=1}^{2} r_i\mathbf{Q}_i^{\mathrm{T}}\mathbf{Q}_i \tag{42}$$

where the diagonal matrix $\mathbf{V}(\mathbf{X}) = \mathrm{diag}\left\{\left[1 + \mathbf{X}_i^2/\sigma_{\mathbf{X}}^2\right]^{-1}\right\}$.

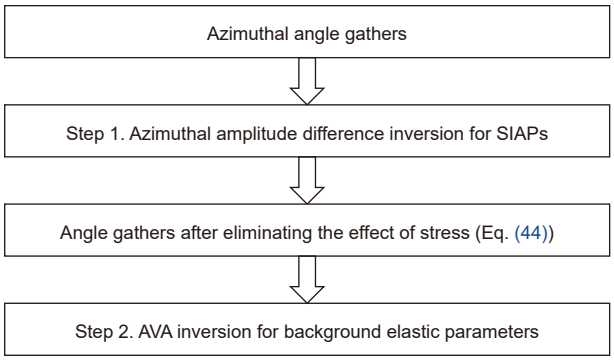

Fig. 7. Stepwise azimuthal amplitude inversion strategy, developed and applied in this paper, for SIAPs and elastic parameters in stress-induced anisotropic media.

Solving Eq. (42) is a nonlinear problem, and the iteratively reweighted least-squares (IRLS) algorithm (Bissantz et al., 2008) is employed; the specific process can be referred to in Algorithm 1. After several iterations, the anisotropic parameter $\mathbf{X}$ can be reasonably estimated.

Algorithm 1. Iteration process of IRLS method to solve Eq. (42).

1) Initialize: Input $\mathbf{d}$. Set $\mathbf{X} = \mathbf{X}_{\text{low}}$, where $\mathbf{X}_{\text{low}}$ is the low-frequency model of Ψ_{N} and Ψ_{T}, which is obtained from well-logging data. Set η, r_i, the maximum iterative number K, and the convergence threshold ε.
2) Construct the operators $\mathbf{G}$ and $\mathbf{Q}$.
3) While $\left\|\mathbf{X}^{k+1} - \mathbf{X}^{k}\right\|^2 > \varepsilon$ do
4) for $i = 1, \ldots, K$
5) $\mathbf{X}^{k+1} = \left[\mathbf{G}^{\mathrm{T}}\mathbf{G} + \sum_{i=1}^{2} r_i \mathbf{Q}_i^{\mathrm{T}}\mathbf{Q}_i + \eta \mathbf{V}\left(\mathbf{X}^{k}\right)\right]^{-1}\left[\mathbf{G}^{\mathrm{T}}\mathbf{d} + \sum_{i=1}^{2} r_i \mathbf{Q}_i^{\mathrm{T}}\mathbf{Q}_i\right]$
6) end
7) end

5.3. Second step: AVA inversion for background elastic parameters

Eq. (26) provides the isotropic PP-wave reflectivity characterized by the relative variations in the P- and S-wave modulus and density, which can be written in natural logarithmic differential form as

$$\frac{\Delta M}{M} \approx \Delta \ln(M) = \Delta X_M, \quad \frac{\Delta \mu}{\mu} \approx \Delta \ln(\mu) = \Delta X_\mu, \quad \frac{\Delta \rho}{\rho} \approx \Delta \ln(\rho) = \Delta X_\rho \tag{43}$$

Once the SIAPs are obtained, the known influence of stress can be subtracted from azimuthal angle gathers through Eq. (25). The forward model of the second step can be expressed as

$$\underbrace{\mathbf{D} - \mathbf{G}^{\phi_0}\mathbf{X}}_{\mathbf{d}'} = \mathbf{G}'\mathbf{X}' \tag{44}$$

where $\mathbf{D}$ is the seismic data with $\phi = 0°$, including h incident angles, and $\mathbf{X}'$ is the inversion parameter and consists of the natural logarithms of M, μ and ρ. The operator $\mathbf{G}^{\phi_0} = \mathbf{G}^{\phi}(\phi = 0°)$ (Eq. (38)) and $\mathbf{G}'$ is the forward operator with respect to M, μ and ρ at $\phi = 0°$.

We imitate the inversion approach of the first-step and introduce the corresponding regularization terms to ensure the accuracy of the inversion results. The objective function is with the same form as Eq. (40), expressed as

$$J_2(\mathbf{X}') = \min_{\mathbf{X}'}\left\{\|\mathbf{d}' - \mathbf{G}'\mathbf{X}'\|_2^2 + \eta' \sum_{i=1}^{3} \ln\left(1 + (\mathbf{X}_i')^2 \Big/ (\sigma_i')^2\right) + \sum_{i=1}^{3} r_i' \|\boldsymbol{\zeta}_i' - \mathbf{Q}_i'\mathbf{X}_i'\|_2^2\right\} \tag{46}$$

Likewise, we take the gradient on both sides of Eq. (46) with respect to $\mathbf{X}'$ and apply the IRLS algorithm to optimize the solution for $\mathbf{X}_M$, $\mathbf{X}_\mu$ and $\mathbf{X}_\rho$. Ultimately, the trace integration method and a few mathematical operations are used to transform the inversion results $\mathbf{X}$ and $\mathbf{X}'$ into the final layer attributes (Ma et al., 2022).

6. Results

6.1. Azimuthal seismic reflection response analysis

In order to gain a more intuitive understanding of the effect of stress-induced changes in microcrack compliance on the seismic response characteristics, the variation of the proposed PP-wave reflection coefficient with incident angle and azimuth under different stress levels are investigated (The negative sign indicates that the stress is compressive). For unstressed media, i.e., the isotropic rock containing randomly distributed and randomly orientated microcracks, the PP-wave reflection coefficient varies only with the incident angle (as shown in Fig. 8(a), (d) and (g)). The anisotropic media induced by horizontal uniaxial stress exhibits the characteristics of an HTI media due to the preferential decrease of microcrack compliance with respect to the applied stress. Therefore, the PP-wave reflection coefficient of the stressed rock varies not only with the incident angle but also with the azimuth (as shown in Fig. 8(b), (e) and (h)). As the stress increases, the decrease degree of microcrack compliance induced by the applied stress leads to the enhancement of elastic anisotropy. The extreme points of the azimuthal reflection curves remain constant with the increasing stress, but the extreme values increase (as shown in Fig. 8(c), (f) and (i)). In addition, the applied horizontal uniaxial stress decreases the critical angle of P-wave incidence, as demonstrated in Fig. 8(a)–(c), Fig. 8(d)–(f), and Fig. 8(g)–(i). In conclusion, horizontal uniaxial stress leads to the preferential decrease of microcrack compliance, which in turn changes the elastic properties of the rock. The amplitude and critical angle of the PP-wave reflection coefficient are affected, but the azimuthal periodicity remains invariant.

$$\mathbf{G}' = \begin{bmatrix} a_M(\theta_1,\phi_0)\mathbf{W}(\theta_1,\phi_0)\mathbf{L} & a_\mu(\theta_1,\phi_0)\mathbf{W}(\theta_1,\phi_0)\mathbf{L} & a_\rho(\theta_1,\phi_0)\mathbf{W}(\theta_1,\phi_0)\mathbf{L} \\ a_M(\theta_2,\phi_0)\mathbf{W}(\theta_2,\phi_0)\mathbf{L} & a_\mu(\theta_2,\phi_0)\mathbf{W}(\theta_2,\phi_0)\mathbf{L} & a_\rho(\theta_2,\phi_0)\mathbf{W}(\theta_2,\phi_0)\mathbf{L} \\ \vdots & \vdots & \vdots \\ a_M(\theta_h,\phi_0)\mathbf{W}(\theta_h,\phi_0)\mathbf{L} & a_\mu(\theta_h,\phi_0)\mathbf{W}(\theta_h,\phi_0)\mathbf{L} & a_\rho(\theta_h,\phi_0)\mathbf{W}(\theta_h,\phi_0)\mathbf{L} \end{bmatrix} \tag{45}$$

$$\mathbf{D} = \begin{bmatrix} \mathbf{d}(\theta_1,\phi_0) & \mathbf{d}(\theta_2,\phi_0) & \cdots & \mathbf{d}(\theta_h,\phi_0) \end{bmatrix}^{\mathrm{T}}, \ \mathbf{X}' = \begin{bmatrix} \mathbf{X}_M & \mathbf{X}_\mu & \mathbf{X}_\rho \end{bmatrix}^{\mathrm{T}}$$

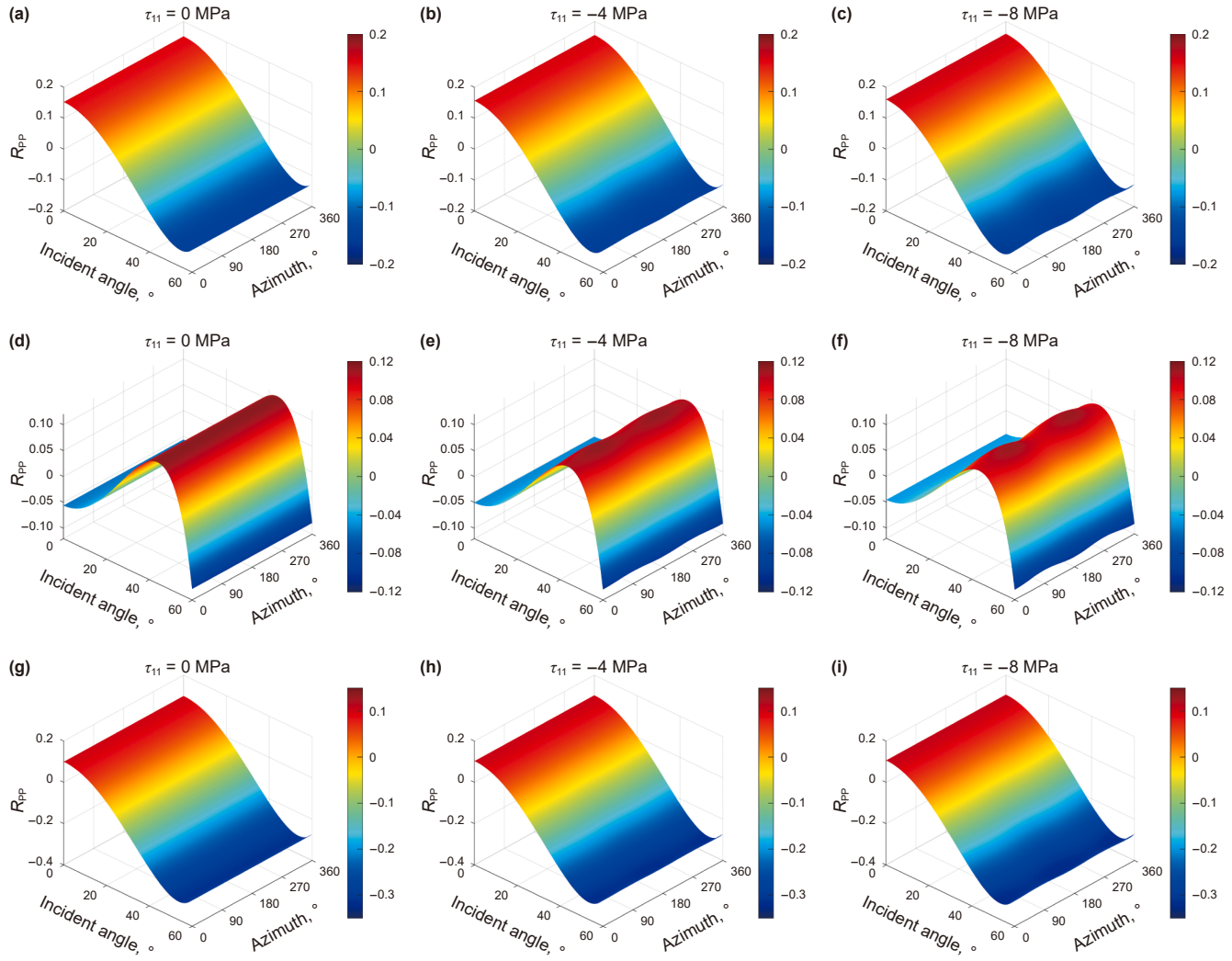

Fig. 8. Variation of PP-wave reflection coefficients with incident angle and azimuth under different horizontal uniaxial stresses. **(a)**–**(c)** The reflection coefficients for an isotropic Mexico A sandstone overlying an isotropic Mexico C sandstone subjected to horizontal uniaxial stress of 0, −4, and −8 MPa, respectively. **(d)**–**(f)** The reflection coefficients for an isotropic Mexico C sandstone overlying an isotropic Penrith sandstone subjected to horizontal uniaxial stress of 0, −4, and −8 MPa, respectively. **(g)**–**(i)** The reflection coefficients for an isotropic Penrith sandstone overlying an isotropic Barre Granite subjected to horizontal uniaxial stress of 0, −4, and −8 MPa, respectively. The elastic properties of rock samples are given in Table 1.

6.2. Model inversion

The feasibility of the azimuthal amplitude inversion method proposed in this article is tested a real model, obtained from field logs. The logging model parameters are calculated by using well logs and rock physics analysis results. The true model parameters of P-wave modulus, shear modulus, density and SIAPs are displayed in black in Fig. 9, which have been filtered to the seismic frequency band. The green lines are the low-frequency models obtained by 8 Hz high-cut filtering.

The PP-wave reflection coefficient is calculated by Eq. (25) and the seismic data with azimuths of 0° and 90° are then synthesized using a Ricker wavelet with a dominant frequency of 30 Hz and a sampling interval of 2 ms. To implement the first-step inversion, the azimuthal amplitude difference is obtained by subtracting two azimuthal seismic records. And by solving Eq. (40), the SIAPs can be estimated, which are then used as inputs for the second step inversion. To further demonstrate the stability of the inversion method, we generate azimuth gathers by adding different Gaussian random noises to the noise-free seismic data to obtain new pre-stack seismic gathers with signal-to-noise ratios (S/Ns) of 8:1 and 4:1, as shown in Fig. 10. And the corresponding inversion results of model parameters are shown in Fig. 11(a), (b) and (c), respectively.

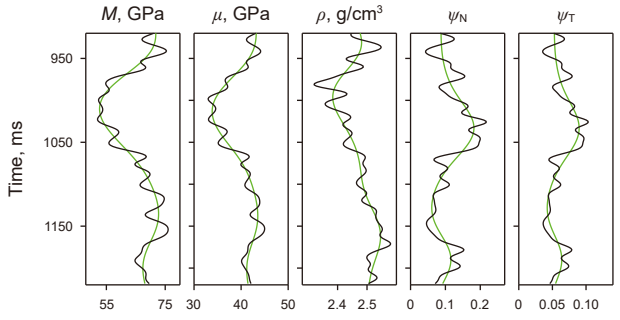

Fig. 9. True models containing P- and S-modulus, density, and two SIAPs, calculated from the proposed rock physics model. The logging curves have been filtered to seismic frequency bands by the high cut (black lines). The green lines are the low-frequency models obtained by 8 Hz high-cut filtering.

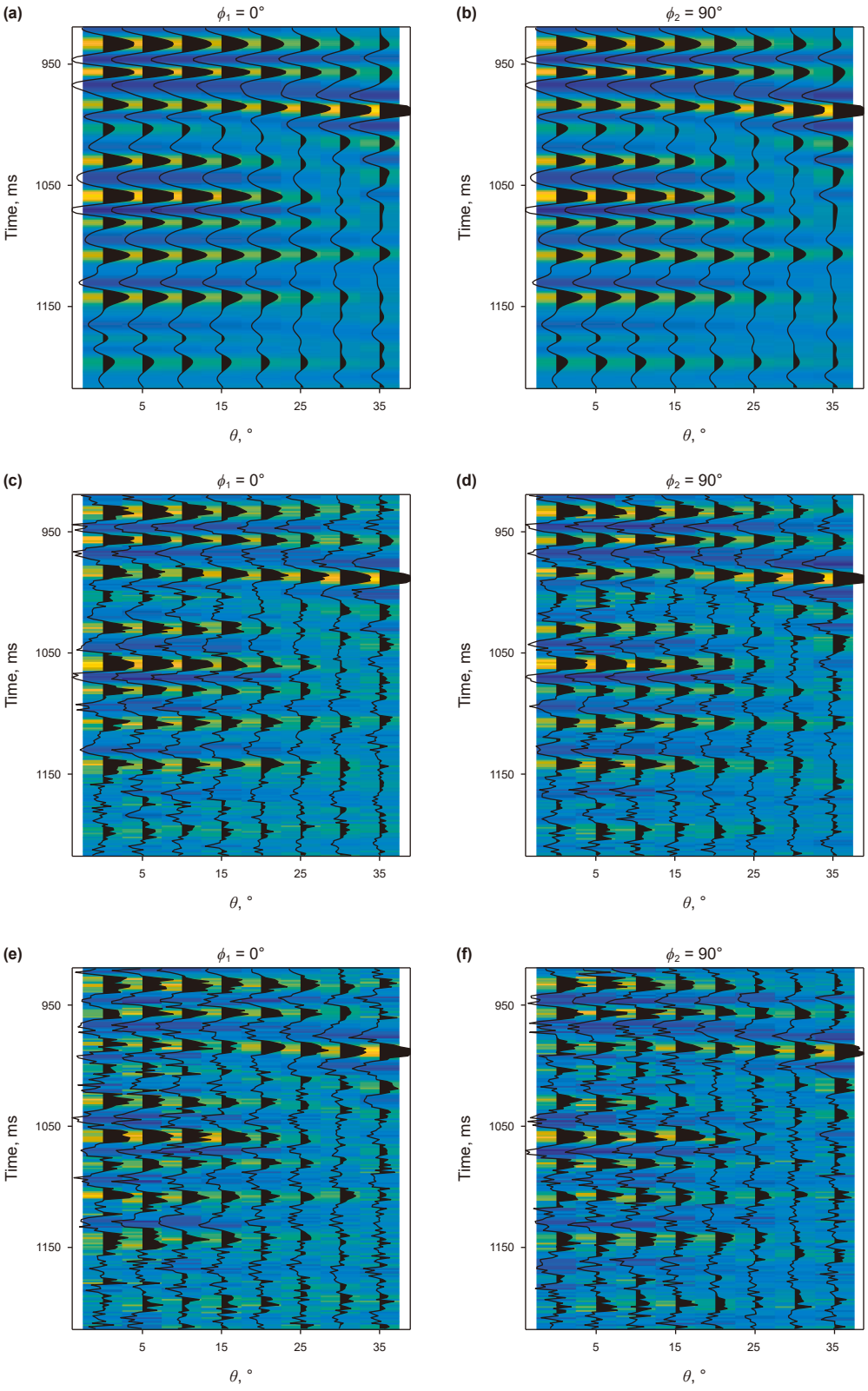

Fig. 10. Synthetic seismic records with azimuths of 0° and 90°: **(a)**–**(b)** noise-free, **(c)**–**(d)** S/N = 8, **(e)**–**(f)** S/N = 4.

The feasibility and robustness of the inversion method are confirmed through relative error analysis of the noise-free and noisy inversion results (Fig. 12). The relative error is calculated by

$$\Gamma = \frac{\|\mathbf{m}_{\text{ture}} - \mathbf{m}_{\text{inv}}\|_2}{\|\mathbf{m}_{\text{inv}}\|_2} \tag{47}$$

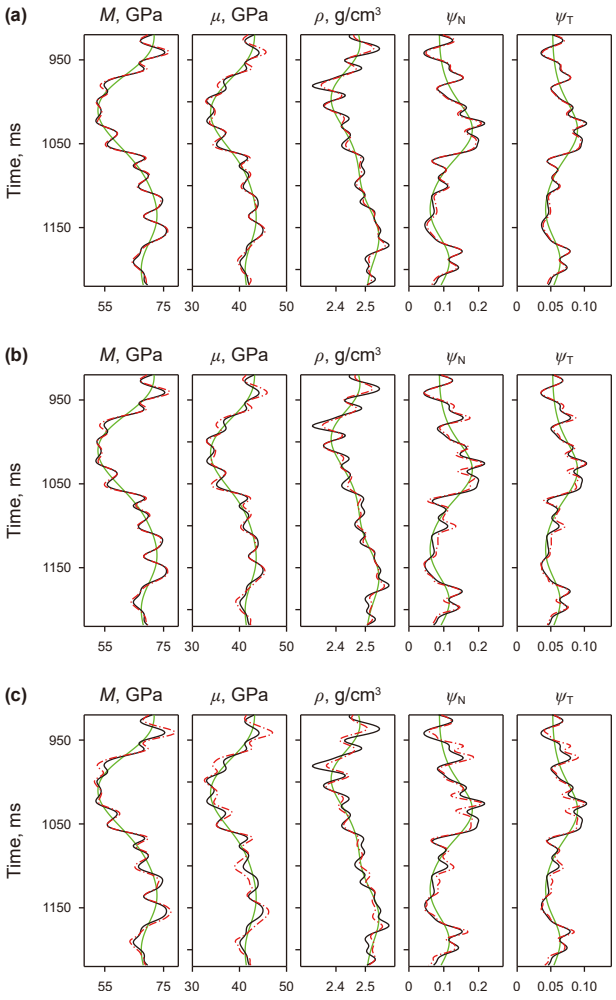

Fig. 11. Inverted model parameters from the seismic data shown in Fig. 10: **(a)** noise-free results correspond to Fig. 10(a)–(b), **(b)** S/N = 8 results correspond to Fig. 10(c) and (d); **(c)** S/N = 4 results correspond to Fig. 10(e) and (f). The black solid lines, green solid lines and red dash lines indicate the true models, initial models and inverted models, respectively.

where $\mathbf{m}_{\text{ture}}$ and $\mathbf{m}_{\text{inv}}$ are the true models and inversion results, respectively. Fig. 12(a)–(c) correspond to the noise-free and noisy inversion results in Fig. 11(a)–(c), respectively. We can observe that the accuracy of inversion result decreases as the noise interference increases. However, there is still a good agreement between the inversion results and the real values, confirming the feasibility and robustness of the inversion method proposed in this article.

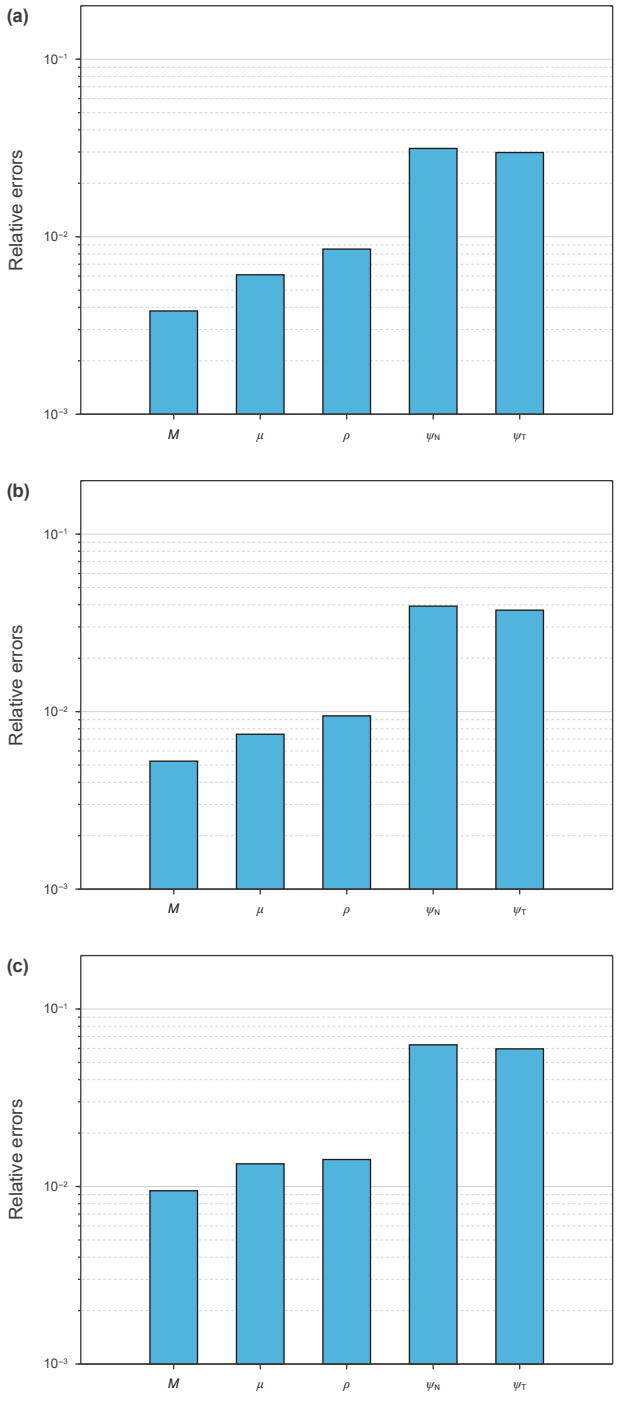

Fig. 12. Relative errors between the inversion results and the true models: **(a)**–**(c)** correspond to the inversion results of Fig. 11(a), (b) and (c), respectively.

6.3. Inversion of field seismic data

We further test the azimuthal amplitude inversion approach suggested in this article on real seismic data. The study area, located in northwestern China, is a sand-shale interbedded reservoir. Based on prior geological knowledge, the target layer is an oil-bearing reservoir, and experiences several tectonic activities with pronounced S_{Hmax}. Through the logging data of a known well (Fig. 13), we can find that the shear wave splitting phenomenon exists. The highlighted shear wave splitting zones have relatively high S_{Hmax}, which is positively correlated with S-wave anisotropy. Therefore, we think that the anisotropy in the study area originates from S_{Hmax}. Meanwhile, the anisotropy azimuth is shown to be 105°, which provides prior information for selecting azimuthal seismic data.

To ensure that the selected azimuthal seismic data can represent the reflected features of the subsurface interface as properly as possible, we have implemented a complete seismic data processing flow, as shown in Table 4. Fig. 14 shows the processed seismic profiles of the selected area with azimuths of 15° and 105°, across well A. The stack incidence angles for each azimuth are 8° (pre-stack angle range is 2°–14°), 18° (pre-stack angle range is 14°–22°) and 28° (pre-stack angle range is 22°–34°). The black dotted line in Fig. 14 represents the location of well A and the area

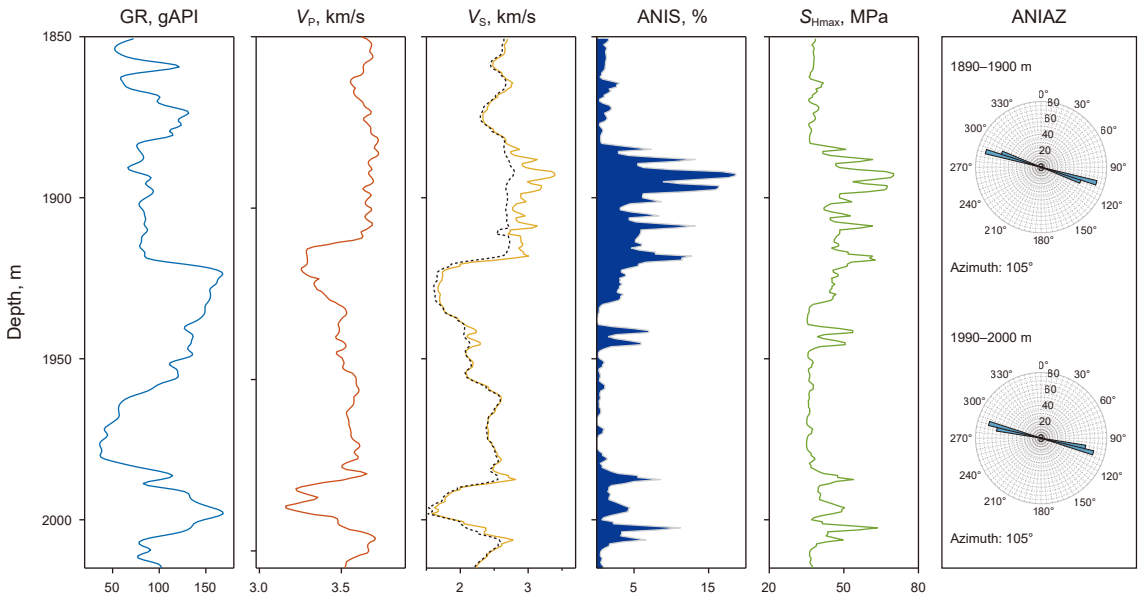

Fig. 13. Well logs of a real well in the study area. These logs are the Gamma ray (GR); P-wave velocity (V_P); S-wave velocity (V_S), where the solid line represents the fast S-wave, and the dotted line represents the slow S-wave; S-wave anisotropy (ANIS); maximum horizontal compressive stress (S_{Hmax}); anisotropy azimuth (ANIAZ) from left to right. Intervals of the bore hole with significantly anomalous physical properties, interpreted to be shear wave splitting zone, are highlighted.

surrounded by the ellipse denotes the target area, which is mainly an oil-water layer. The rock physical modelling process for the target area follows Fig. 4, and the well curves for model parameters can be calculated. We then construct the initial low-frequency models of model parameters by interpolating, extrapolating, and smoothing the logging data along the layer, as shown in Fig. 15. The azimuthal difference seismic wavelets are extracted through the azimuthal amplitude difference between the two azimuths, as shown in Fig. 16(a). Subsequently, we perform the first-step inversion for SIAPs, as shown in Fig. 17.

Next, we take the estimated SIAPs as inputs to obtain angle gathers after eliminating the effect of stress through Eq. (44). The extracted seismic wavelets at three angles are shown in Fig. 16(b), which are used to estimate the remaining isotropic parameters through the second-step inversion process, as displayed in Fig. 17. From the inversion profiles in Fig. 17, it can be seen that P- and S-wave modulus and density near the target layer both show low values, which is contrast to the high value anomalies of SIAPs. Due to the oil-bearing nature of the reservoir, this phenomenon can be explained by the Brown-Korringa formula (Brown and Korringa, 1975).

To validate the reliability of our proposed inversion approach, we present the comparisons between the inversion results and the well logs estimated from the well log interpretations and rock physics analysis at well location, as displayed in Fig. 18. It can be seen that inversion results (red dashed lines) show an acceptable agreement with the logging curves (black solid lines). The accuracy of the proposed method is tested by calculating the relative error between the inversion results and the logging curves through Eq. (47), as shown in Fig. 19. Compared with the elastic parameters, the inversion results of anisotropic parameters have slightly larger errors, but the accuracy is still within acceptable limits. In terms of verifying stress-induced anisotropy, we further draw the cross-plots between SIAPs and S_{Hmax}, as displayed in Fig. 20. We can see that SIAPs have the potential to indicate S_{Hmax}.

Finally, we apply the proposed method to the 3D work area and extracted the root-mean-square slices of estimated model parameters along the target layer, as shown in Fig. 21. Fig. 21(a)–(e) show the slices of the inverted P-wave modulus, shear modulus, density, and SIAPs, and they are in good agreement with seismic amplitude of Fig. 21(f). The black dot indicates the location of the known well A. Around the well, the predicted P- and S-wave modulus and density show low values, but SIAPs show high values, which is consistent with the prior knowledge. The application of field seismic data verifies the effectiveness and feasibility of the proposed method. Therefore, we conclude that the inversion method suggested in this article can provide a reasonable estimation of the model parameters in stress-induced anisotropic media.

7. Discussion

We implement azimuthal amplitude inversion in a horizontal uniaxial stress-induced anisotropic media using a novel PP-wave reflection coefficient that incorporates the effect of stress on microcrack compliance. An analytical model, similar to the results of Gurevich et al. (2011), is proposed to elucidate the anisotropy induced by horizontal uniaxial stress applied to an initially isotropic elastic media. Instead of invoking an exponential dependence of the area of the displacement microcracks with respect to the applied stress, we account for stress-induced anisotropy through the stress-dependence of microcrack compliance. In contrast to the TOE theory, the effect of stress on rock microstructure is considered (as demonstrated in Eqs. (8) and (9)), allowing for a complete rock physical modelling process for the stress-induced anisotropic media (as shown in Fig. 4). Various approximate assumptions are used in the derivation process, and clarifying these assumptions will be useful for understanding the rationale behind them and their validity.

1) The rock is modeled as an elastic material, implying the exclusion of any anelastic and irreversible deformations. While this assumption is widely adopted in geophysical studies, it should be noted that such an idealization may not be universally valid for all rock types in nature. Nevertheless, for well-consolidated rocks under low-stress conditions, this elastic

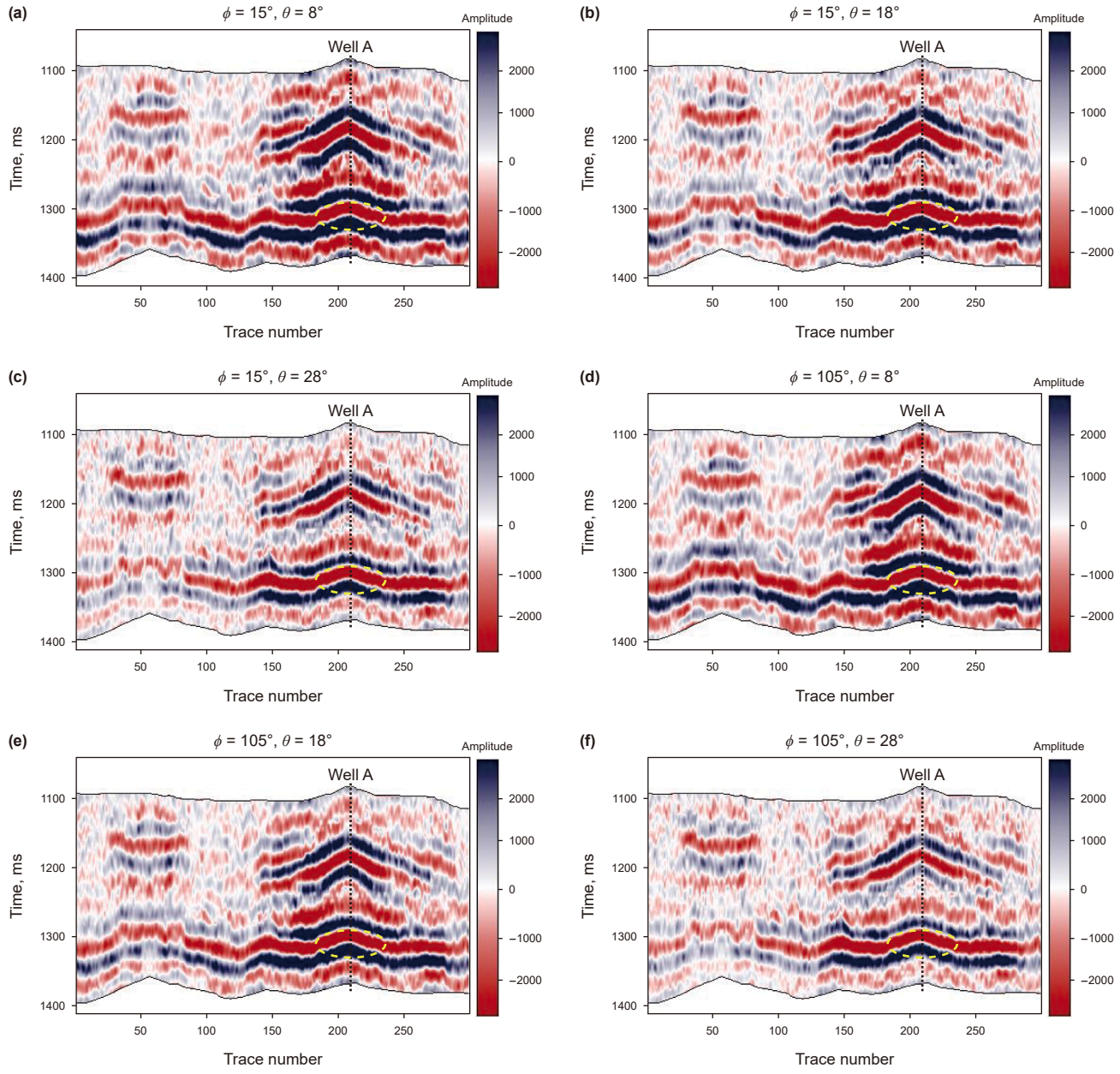

Fig. 14. Partial angle-stacked seismic profiles across a known well (indicated by black dotted line) with azimuth $\phi = 15°, 105°$ and incident angle $\theta = 8°, 18°, 28°$.

approximation remains theoretically justified and practically applicable.

2) Our model represents the unstressed media as an elastic, isotropic media containing randomly oriented microcracks. Such a model is an idealization for most rocks, which are collections of grains individually exhibiting elastic, anisotropic behavior. Although the deformation of individual grain is decidedly anisotropic, behavior of a large group of grains may be considered isotropic if the grains have no preferred orientation. Crucially, if the rock is isotropic, the microcracks that significantly influence deformation behavior, must demonstrate random spatial orientations.
3) We assume that microcrack compliance decreases exponentially with increasing stress. This assumption is inspired by the progressive increase in contact area between opposing microcrack surfaces under growing compressive stress. We are not the first to propose this assumption; see Shapiro and Kaselow (2005), Gurevich et al. (2011) and Sayers et al. (2024). This assumption is clearly not universally valid, and a matter behind this assumption is about whether microcrack opening occurs. This limitation represents an important area for future development of our model. Furthermore, the microcrack compliance is usually assumed to depend solely on the normal component of effective stress acting on the microcrack plane, which may imply that the unstressed media is dry. But as discussed by Gurevich et al. (2011), it can be applied to fluid-saturated rocks if the fluid-filled microcracks are hydraulically isolated. In the rock physics modelling process, we use the anisotropic Gassmann

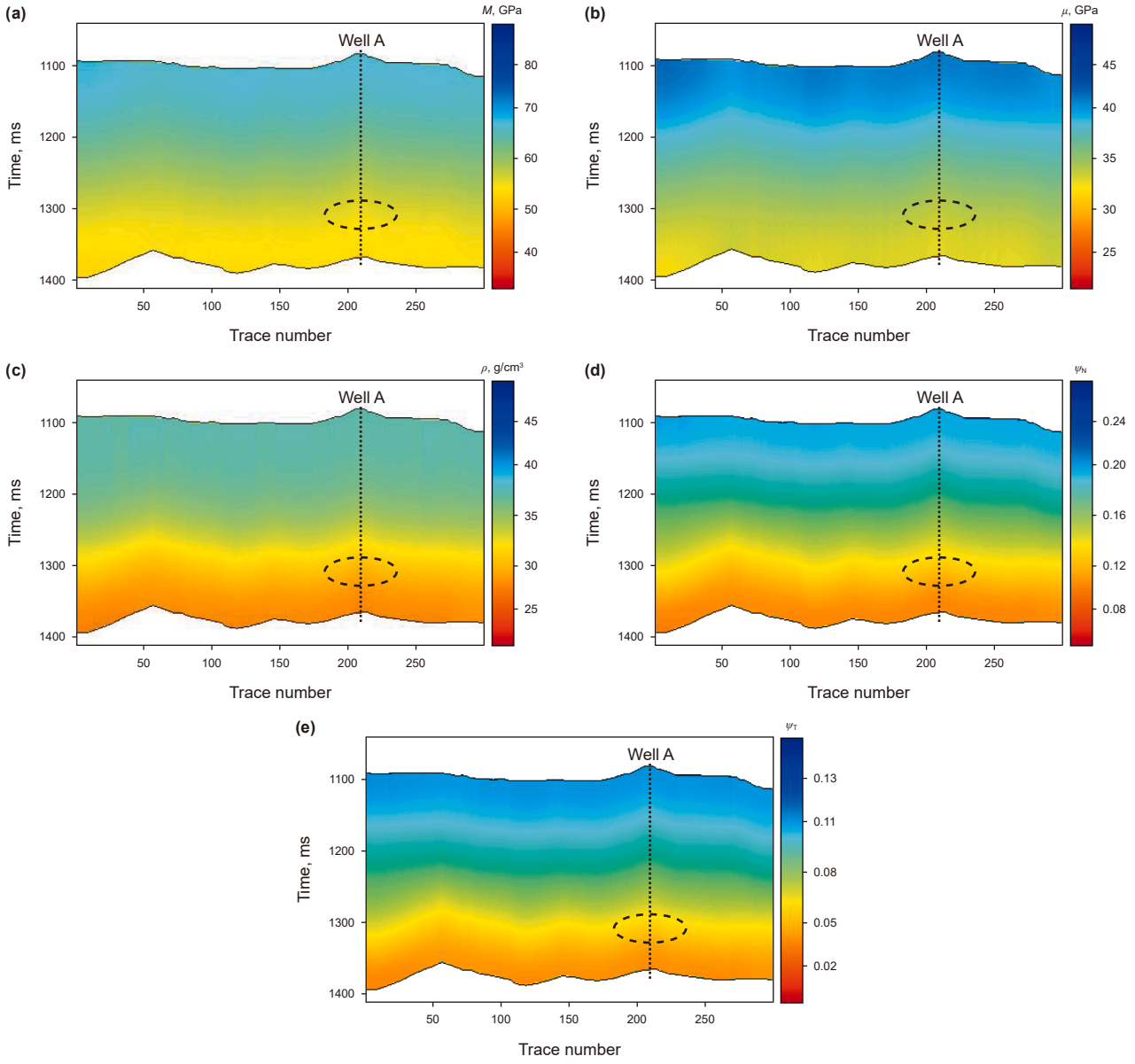

Fig. 15. Initial low-frequency models for **(a)** M, **(b)** μ, **(c)** ρ, **(d)** Ψ_N, and **(e)** Ψ_T, obtained by interpolating, extrapolating and smoothing the logging curves along the layers.

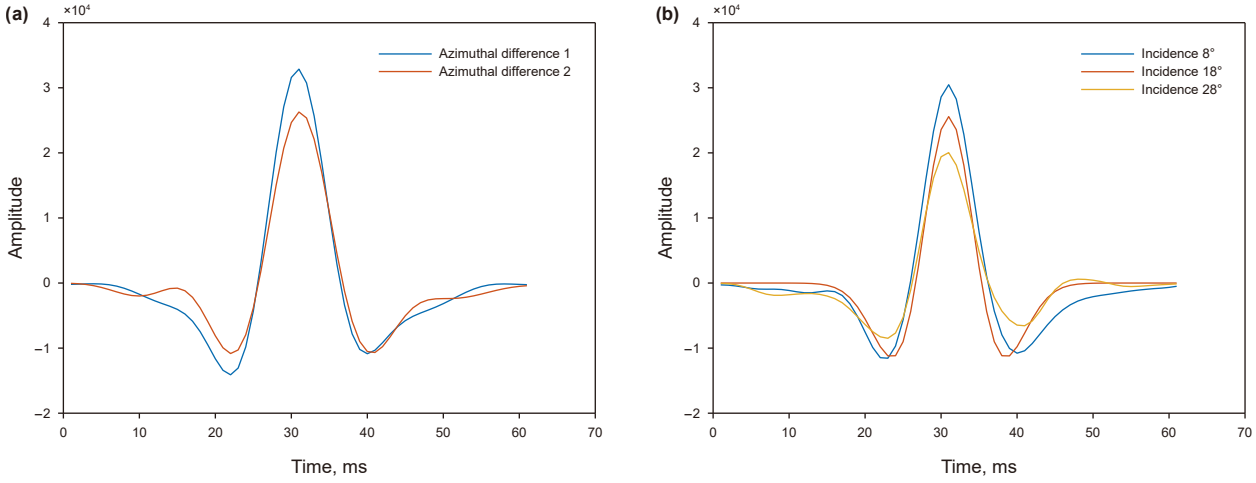

Fig. 16. Extracted seismic wavelets for stepwise azimuthal amplitude inversion: **(a)** Azimuthal difference seismic wavelets for the first-step inversion, **(b)** angle gather seismic wavelets for the second-step inversion.

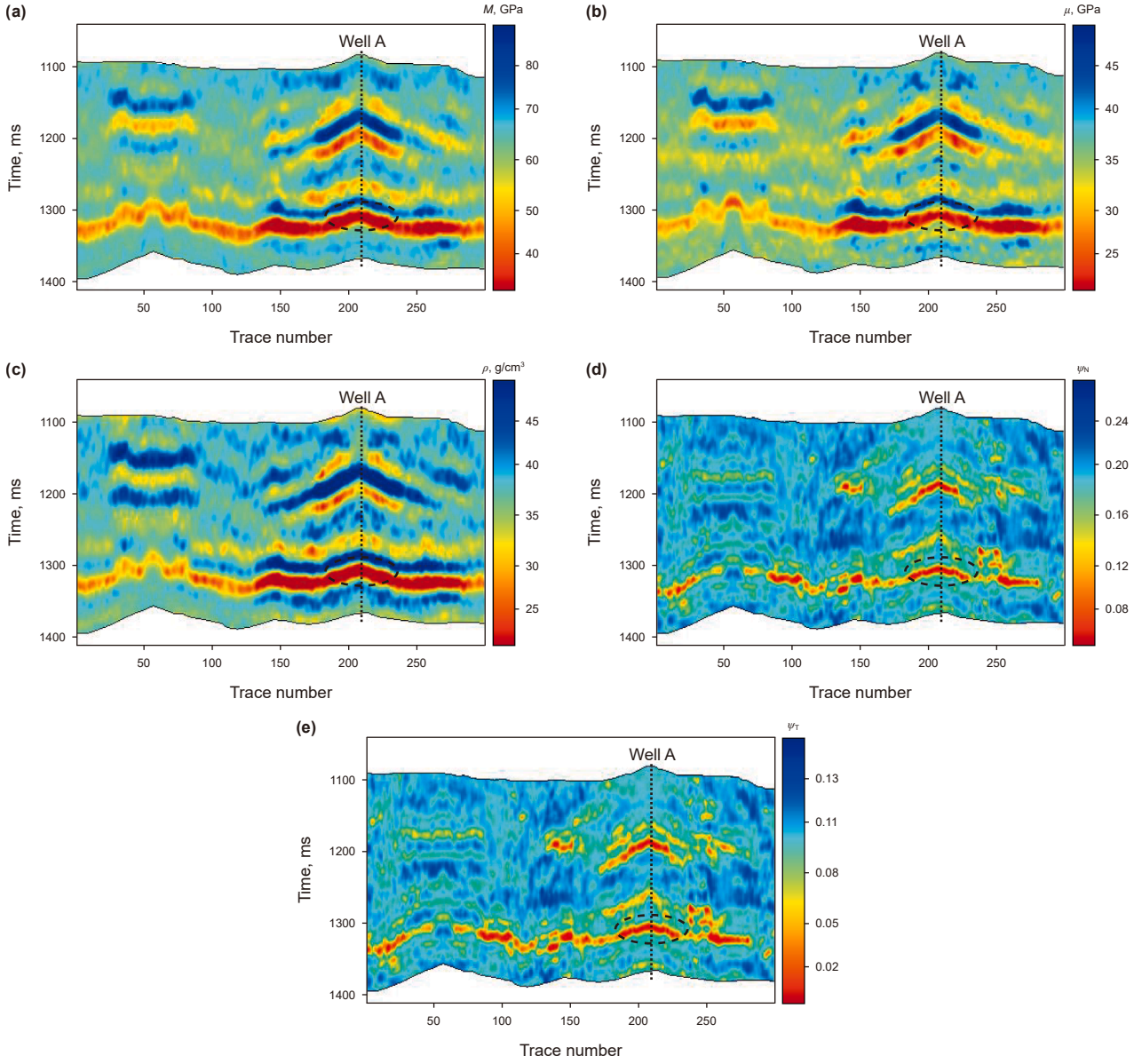

Fig. 17. Inverted profiles of model parameters: **(a)** M, **(b)** μ, **(c)** ρ, **(d)** Ψ_N, **(e)** Ψ_T. The black dotted lines indicate the path of a known well and the location of the reservoir is circled by the ellipse.

equation (Brown and Korringa, 1975) to compute the effect of fluid saturation. However, for higher frequencies, the frequency-dependent dispersion caused by wave-induced fluid flow (WIFF) between microcracks and pores may need to be considered, such as the squirt-flow model (Gurevich et al., 2010).

4) The assumption of rotationally invariant microcrack implies that microcrack compliance matrix in the coordinate system convenient to the microcracks depends on two compliances, a normal compliance Ω_N and a tangential compliance Ω_T. And it does not mean that microcracks are circular in shape, but rather that microcracks oriented parallel to a certain plane have random orientations in that plane.
5) We use the linearization expressions of the exponential decay for microcrack compliance, as shown Eqs. (5) and (6). Under this assumption, the properties of the uniaxially stressed rock (such as compliance, stiffness, and seismic wave velocity) vary linearly with stress. The applied stress is assumed to be small compared to the microcrack closing pressure. Such weak stress

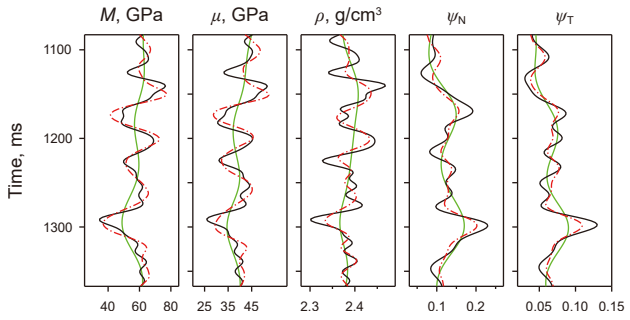

Fig. 18. Comparison of well curves (black solid lines) and inverted results (red dashed lines) at well location. The black solid lines, green solid lines and red dash lines indicate the true models, initial models and inverted models, respectively.

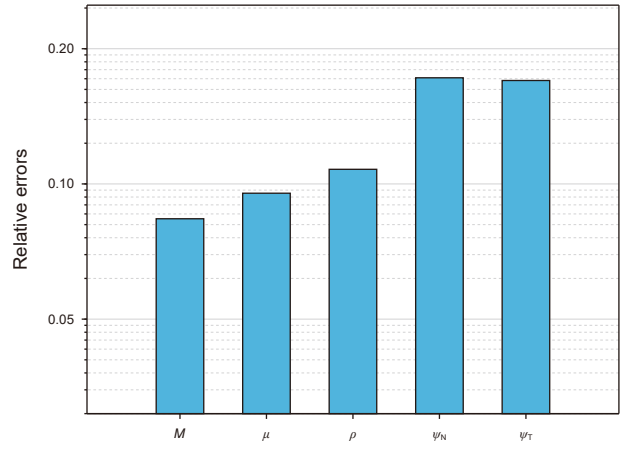

Fig. 19. Relative errors between inversion results and logging curves.

assumption will fail as the stress increases, and the higher-order Taylor expansion of the exponential functions is required. But the corresponding stress-induced anisotropy model will be very complicated and difficult to be used for practical seismic inversion.

When constructing the stiffness tensor of the uniaxial-stress-induced anisotropic media, two SIAPs, i.e., Ψ_N and Ψ_T, are introduced to describe the strength of stress-induced normal and tangential anisotropy, respectively. Contrary to the physical meaning of the fracture weakness parameters (Bakulin et al., 2000), which are defined as the weakening effect of fractures on the rock, the SIAPs can be regarded as parameters describing the stiffening effect of compressive stress on the rock. Larger SIAPs imply that the region is subjected to larger S_{Hmax}, i.e., higher anisotropy.

For stress-induced anisotropy inversion, it is inherently a multi-parameter problem. We propose a stepwise inversion strategy based on the characteristics of the azimuthal anisotropy to improve the accuracy of inversion results. However, it is worth noting that the results of the first-step have a considerable impact on the second-step. During the process of each inversion step, an initial trade-off between the model parameters is usually given based on their contributions (as shown in Fig. 6) and then slowly adjusted.

Furthermore, the inducements of seismic anisotropy are diverse, and it is difficult to fully determine whether seismic anisotropy is caused by in-situ stress. In this study, the shear wave splitting, the correlation between shear wave anisotropy and S_{Hmax}, and the cross-plots between the inverted SIAPs and S_{Hmax} can be used to prove stress-induced anisotropy. However, the assumption that the anisotropy is thoroughly stress-induced may have difficulty describing some exceptional cases, such as the intrinsic anisotropy (Pan and Zhao, 2024). In field data, the two factors are strongly coupled, and how to differentiate stress-induced anisotropy from other types presents a challenge. Although seismic anisotropy is closely related to S_{Hmax} in some regions, the subsurface stress field is quite complex, and considering only horizontal uniaxial stress may not accurately characterize the stress state of the rock. Therefore, we intend to consider the normal stress traction acting on the microcrack surface for triaxial stress loading, and construct triaxial stress-induced anisotropy model. It should also be noted that stress orientation is a significant parameter. We use the anisotropy azimuth from imaging logging to indicate stress orientation. In recent years, scholars have conducted extensive research on prediction of stress orientation, such as the focal mechanism solutions (FMSs)

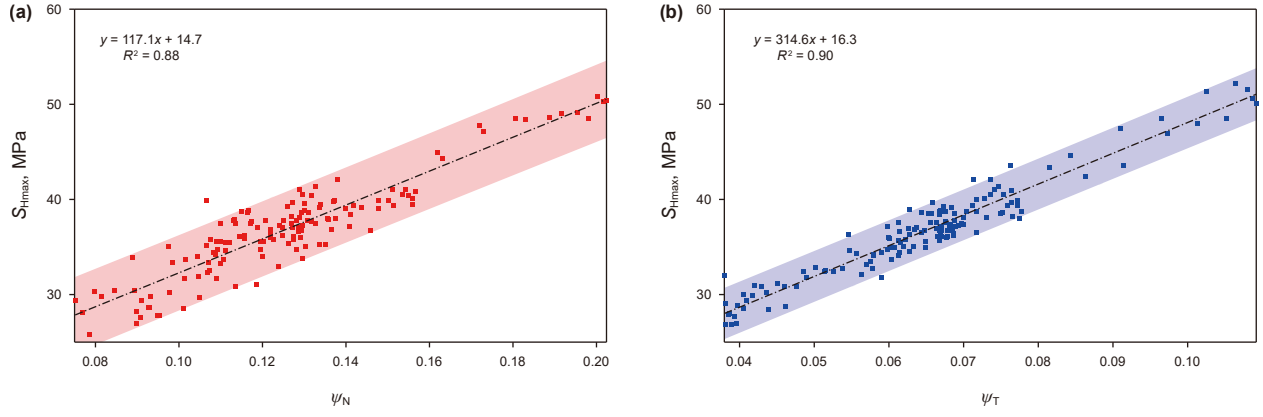

Fig. 20. Correlations between S_{Hmax} and SIAPs: **(a)** Ψ_N, **(b)** Ψ_T. The red and blue bands represent the 95% prediction confidence intervals.

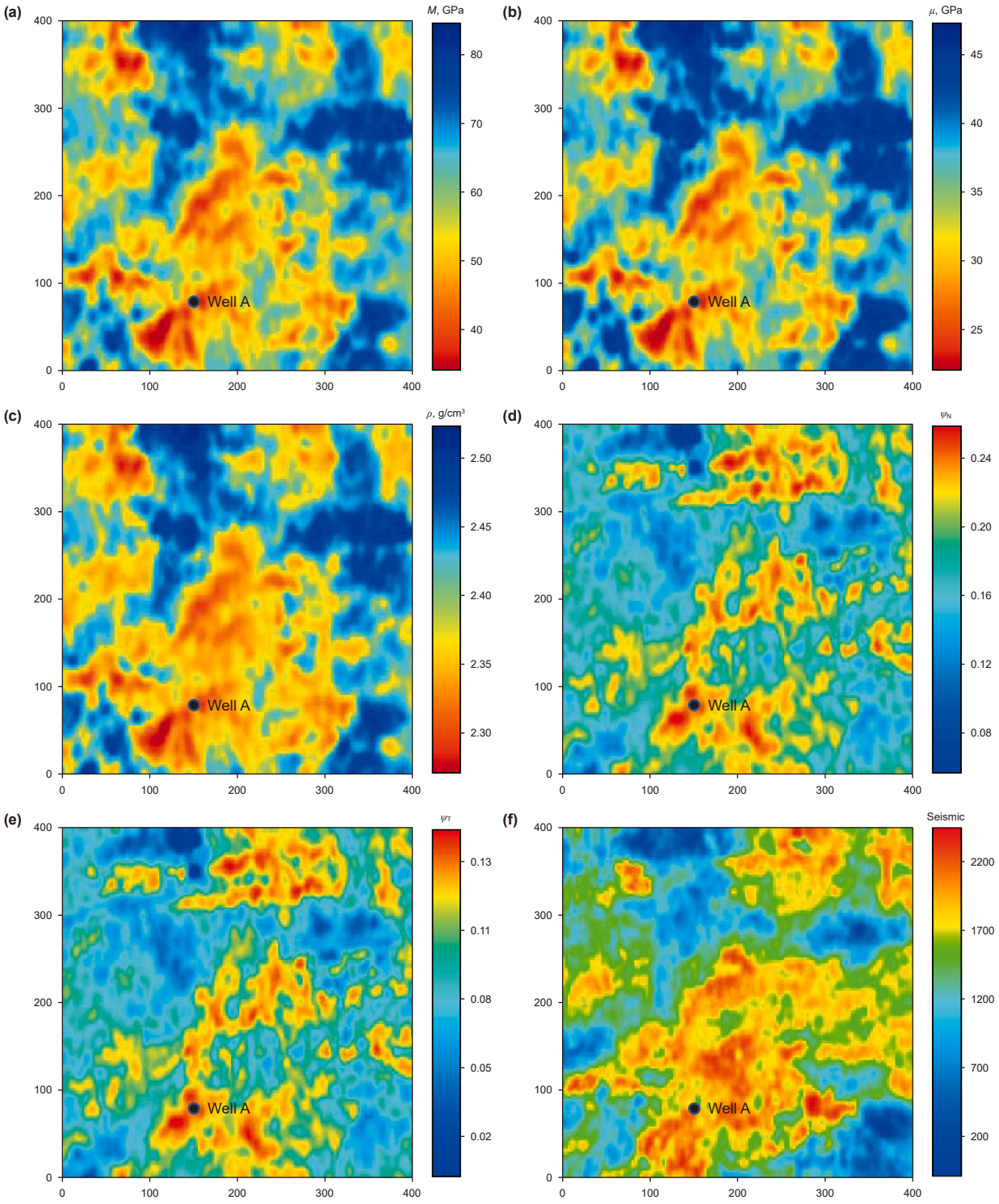

Fig. 21. Root-mean-square slices along the target layer with different data. **(a)** P-wave modulus, **(b)** shear modulus, **(c)** density, **(d)** Ψ_N, **(e)** Ψ_T, **(f)** seismic.

(Heidbach et al., 2018), machine learning (ML) methods (Lyu et al., 2024) and multi-scale data joint estimation method (Cao et al., 2025). Therefore, further research should revolve around reconstructing the 3D stress field based on the mechanism of stress-induced anisotropy.

8. Conclusion

The presented methodology focuses on an incorporation case of azimuthal amplitude inversion with rock physics model in isotropic elastic media subjected to uniaxial compression. An analytical model is proposed to explain stress-induced anisotropy from the perspective of stress-dependence of microcrack compliance, and then used to establish the effective elastic stiffness tensor of the uniaxial-stress-induced anisotropic media under the assumption of weak anisotropy. Subsequently, using the perturbation tensor and the scattering function, we derived a linearized PP-wave reflection coefficient in terms of P- and S-wave moduli, density and two defined SIAPs. Numerical results illustrate how the reflection coefficients are affected by horizontal uniaxial stress. Finally, combining the derived reflection coefficient and azimuthal amplitude difference inversion with the Cauchy-sparse and low-frequency information regularization, the SIAPs and elastic parameters are estimated stepwise from azimuthal seismic data demonstrated using both a well-logging-based synthetic test and field seismic data.

CRediT authorship contribution statement

Liang-Yi Deng: Writing – original draft, Visualization, Software, Methodology, Conceptualization. **Xing-Yao Yin:** Writing – review & editing, Methodology. **Kun Li:** Writing – review & editing, Validation. **Zheng-Qian Ma:** Writing – review & editing, Formal analysis. **Ya-Ming Yang:** Writing – review & editing, Visualization.

Declaration of competing interest

We declare that we do not have any commercial or associative interest that represents a conflict of interest in connection with the work submitted.

Acknowledgements

We would like to acknowledge the sponsorship of National Natural Science Foundation of China (42430809, 42404132, 42274157), the Fund of State Key Laboratory of Deep Oil and Gas, China University of Petroleum (East China) (SKLDOG2024-ZYTS-02), the Postdoctoral Fellowship Program of CPSF (GZB20240850), the Postdoctoral Project of Qingdao (QDBSH20240102082), the Fundamental Research Funds for the Central Universities (24CX07004A, 24CX06036A), and the China Postdoctoral Science Foundation (2025M770385). Liang-Yi Deng would also like to thank Prof. Boris Gurevich and Prof. Colin M. Sayers for their insightful answers about stress-induced anisotropy.

Appendix A. Evaluation of excess compliance tensors

Calculating the spherical integrals with the software Mathematica in Eqs. (3) and (4), the components of the second- and fourth-rank tensors are obtained as follows:

$$\begin{aligned}\alpha_{11} &= \frac{\Omega_{T0}}{3} - \frac{\Omega_{T0}}{5}\frac{\tau_{11}}{P_{Tc}}\\ \alpha_{22} = \alpha_{33} &= \frac{\Omega_{T0}}{3} - \frac{\Omega_{T0}}{15}\frac{\tau_{11}}{P_{Tc}}\end{aligned} \tag{A-1}$$

$$\begin{aligned}\beta_{1111} &= \frac{(\Omega_{N0}-\Omega_{T0})}{5} - \frac{\Omega_{N0}}{7}\frac{\tau_{11}}{P_{Nc}} + \frac{\Omega_{T0}}{7}\frac{\tau_{11}}{P_{Tc}},\ \beta_{2222} = \frac{(\Omega_{N0}-\Omega_{T0})}{5} - \frac{\Omega_{N0}}{35}\frac{\tau_{11}}{P_{Nc}} + \frac{\Omega_{T0}}{35}\frac{\tau_{11}}{P_{Tc}}\\ \beta_{3333} &= \frac{(\Omega_{N0}-\Omega_{T0})}{5} - \frac{\Omega_{N0}}{35}\frac{\tau_{11}}{P_{Nc}} + \frac{\Omega_{T0}}{35}\frac{\tau_{11}}{P_{Tc}},\ \beta_{1122} = \frac{(\Omega_{N0}-\Omega_{T0})}{15} - \frac{\Omega_{N0}}{35}\frac{\tau_{11}}{P_{Nc}} + \frac{\Omega_{T0}}{35}\frac{\tau_{11}}{P_{Tc}}\\ \beta_{1133} &= \frac{(\Omega_{N0}-\Omega_{T0})}{15} - \frac{\Omega_{N0}}{35}\frac{\tau_{11}}{P_{Nc}} + \frac{\Omega_{T0}}{35}\frac{\tau_{11}}{P_{Tc}},\ \beta_{2233} = \frac{(\Omega_{N0}-\Omega_{T0})}{15} - \frac{\Omega_{N0}}{105}\frac{\tau_{11}}{P_{Nc}} + \frac{\Omega_{T0}}{105}\frac{\tau_{11}}{P_{Tc}}\end{aligned} \tag{A-2}$$

where all other components of tensor $\boldsymbol{\alpha}_{ij}$ are zero. Tensor $\boldsymbol{\beta}_{ijkl}$ is symmetric with respect to all rearrangements of the indices, i.e., $\boldsymbol{\beta}_{ijkl} = \boldsymbol{\beta}_{jikl} = \boldsymbol{\beta}_{ikjl} = \boldsymbol{\beta}_{lkji}\cdots$. For an isotropic media subjected to uniaxial stress, the axial symmetry is considered. Therefore, the nonvanishing components of tensor $\boldsymbol{\beta}_{ijkl}$ are the symmetries of β_{1111}, β_{2222}, β_{3333}, β_{1122}, β_{2233} and β_{1133}.

For the convenience of analysis, we rewrite the excess compliance tensor $\Delta\mathbf{S}_{ijkl}$ in Eq. (1) in the form of a 6×6 tensor using Voigt notation: $ii \to i$, $ij \to 9 - i - j$ $(i \neq j)$ $(i, j = 1, 2, 3)$ while the factors 2 and 4 are introduced as follows: $\Delta\mathbf{S}_{ijkl} \to \Delta\mathbf{S}_{pq}$ when both p and q are 1, 2, 3, $2\Delta\mathbf{S}_{ijkl} \to \Delta\mathbf{S}_{pq}$ when one of p and q is 4, 5, 6, and $4\Delta\mathbf{S}_{ijkl} \to \Delta\mathbf{S}_{pq}$ when both p and q are 4, 5, 6 (Sayers, 2002). Consequently, the excess compliance tensor $\Delta\mathbf{S}_{ij}$ (the 6×6 tensor form) in Eq. (1) can be computed as

$$\begin{aligned}&\Delta S_{11} = \alpha_{11} + \beta_{1111}, \Delta S_{12} = \beta_{1122}\\ &\Delta S_{13} = \beta_{1133},\ \Delta S_{21} = \beta_{2211}\\ &\Delta S_{22} = \alpha_{22} + \beta_{2222},\ \Delta S_{23} = \beta_{2233}\\ &\Delta S_{31} = \beta_{3311},\ \Delta S_{32} = \beta_{3322}\\ &\Delta S_{33} = \alpha_{33} + \beta_{3333},\ \Delta S_{44} = \alpha_{22} + \alpha_{33} + 4\beta_{2233}\\ &\Delta S_{55} = \alpha_{11} + \alpha_{33} + 4\beta_{1133},\ \Delta S_{66} = \alpha_{11} + \alpha_{22} + 4\beta_{1122}\end{aligned} \tag{A-3}$$

where all other components of $\Delta\mathbf{S}_{ij}$ are zero. Combining Eqs. (A-1)–(A-3), the excess compliance tensor $\Delta\mathbf{S}_{ij}$ of the anisotropic media induced by uniaxial stress can be obtained. To distinguish between the isotropic and anisotropic parts of $\Delta\mathbf{S}_{ij}$, we give the resulting tensor in the form as

$$\Delta\mathbf{S}_{ij} = \Delta\mathbf{S}_{ij}^{iso} + \tau_{11-N}\Delta\mathbf{S}_{ij}^{ani-N} + \tau_{11-T}\Delta\mathbf{S}_{ij}^{ani-T} \tag{A-4}$$

where

$$\Delta \mathbf{S}^{\mathrm{iso}} = \Omega_{\mathrm{N0}} \begin{bmatrix} \frac{1}{5} & \frac{1}{15} & \frac{1}{15} & 0 & 0 & 0 \\ \frac{1}{15} & \frac{1}{5} & \frac{1}{15} & 0 & 0 & 0 \\ \frac{1}{15} & \frac{1}{15} & \frac{1}{5} & 0 & 0 & 0 \\ 0 & 0 & 0 & \frac{4}{15} & 0 & 0 \\ 0 & 0 & 0 & 0 & \frac{4}{15} & 0 \\ 0 & 0 & 0 & 0 & 0 & \frac{4}{15} \end{bmatrix} + \Omega_{\mathrm{T0}} \begin{bmatrix} \frac{2}{15} & -\frac{1}{15} & -\frac{1}{15} & 0 & 0 & 0 \\ -\frac{1}{15} & \frac{2}{15} & -\frac{1}{15} & 0 & 0 & 0 \\ -\frac{1}{15} & -\frac{1}{15} & \frac{2}{15} & 0 & 0 & 0 \\ 0 & 0 & 0 & \frac{2}{5} & 0 & 0 \\ 0 & 0 & 0 & 0 & \frac{2}{5} & 0 \\ 0 & 0 & 0 & 0 & 0 & \frac{2}{5} \end{bmatrix} \tag{A-5}$$

is the excess compliance tensor of the isotropic distribution of microcracks in the unstressed rock, and

$$\Delta \mathbf{S}^{\mathrm{ani-N}} = -\Omega_{\mathrm{N0}} \begin{bmatrix} \frac{1}{7} & \frac{1}{35} & \frac{1}{35} & 0 & 0 & 0 \\ \frac{1}{35} & \frac{1}{35} & \frac{1}{105} & 0 & 0 & 0 \\ \frac{1}{35} & \frac{1}{105} & \frac{1}{35} & 0 & 0 & 0 \\ 0 & 0 & 0 & \frac{4}{105} & 0 & 0 \\ 0 & 0 & 0 & 0 & \frac{4}{35} & 0 \\ 0 & 0 & 0 & 0 & 0 & \frac{4}{35} \end{bmatrix} \tag{A-6}$$

is the excess compliance contribution to the decrease in normal compliances of microcracks due to the application of horizontal uniaxial stress, and

$$\Delta \mathbf{S}^{\mathrm{ani-T}} = -\Omega_{\mathrm{T0}} \begin{bmatrix} \frac{2}{35} & -\frac{1}{35} & -\frac{1}{35} & 0 & 0 & 0 \\ -\frac{1}{35} & \frac{4}{105} & -\frac{1}{105} & 0 & 0 & 0 \\ -\frac{1}{35} & -\frac{1}{105} & \frac{4}{105} & 0 & 0 & 0 \\ 0 & 0 & 0 & \frac{2}{21} & 0 & 0 \\ 0 & 0 & 0 & 0 & \frac{16}{105} & 0 \\ 0 & 0 & 0 & 0 & 0 & \frac{16}{105} \end{bmatrix} \tag{A-7}$$

is the excess compliance contribution to the decrease in tangential compliances of microcracks due to the application of horizontal uniaxial stress, and the normalized stresses $\tau_{11\text{-N}}$ and $\tau_{11\text{-T}}$ are given by $\tau_{11-\mathrm{N}} = \tau_{11}/P_{\mathrm{Nc}}$ and $\tau_{11-\mathrm{T}} = \tau_{11}/P_{\mathrm{Tc}}$, respectively.

Appendix B. Effective stiffness tensor of anisotropic media induced by horizontal uniaxial stress

Substituting Eqs. (20) and (21) into Eqs. (15)–(19), the elastic stiffness tensor components of the anisotropic media induced by horizontal uniaxial stress can be represented as

$$C_{11} = M + \left(\frac{8\chi}{105}\lambda + \frac{4}{35}\lambda + \frac{1}{7}M\right)\Psi_{\mathrm{N}} + \left(\frac{2\chi}{35g}\lambda - \frac{4}{35g}\lambda + \frac{2}{35g}M\right)\Psi_{\mathrm{T}} \tag{B-1}$$

$$C_{12} = \lambda + \left(\frac{2\chi}{21}\lambda + \frac{22}{105}\lambda + \frac{1}{35}M\right)\Psi_{\mathrm{N}} + \left(-\frac{1\chi}{35g}\lambda + \frac{2}{35g}\lambda - \frac{1}{35g}M\right)\Psi_{\mathrm{T}} \tag{B-2}$$

$$C_{22} = M + \left(\frac{8\chi}{35}\lambda + \frac{8}{105}\lambda + \frac{1}{35}M\right)\Psi_{\mathrm{N}} + \left(\frac{4\chi}{105g}\lambda - \frac{8}{105g}\lambda + \frac{4}{105g}M\right)\Psi_{\mathrm{T}} \tag{B-3}$$

$$C_{44} = \mu + \frac{4g}{105}\mu\Psi_{\mathrm{N}} + \frac{2}{21}\mu\Psi_{\mathrm{T}} \tag{B-4}$$

$$C_{55} = \mu + \frac{4g}{35}\mu\Psi_{\mathrm{N}} + \frac{16}{105}\mu\Psi_{\mathrm{T}} \tag{B-5}$$

where $g = \mu/M$ and $\chi = \lambda/M$.

Considering the weak perturbations of P-wave modulus, shear modulus, Lamé parameters and SIAPs across the interface separating two distinct anisotropic media induced by horizontal uniaxial stress, the elements of the perturbed effective elastic stiffness tensor can be obtained by neglecting the terms proportional to $\Psi_{\mathrm{N}}\Delta M$, $\Psi_{\mathrm{N}}\Delta\lambda$, $\Psi_{\mathrm{N}}\Delta\mu$, $\Psi_{\mathrm{T}}\Delta M$, $\Psi_{\mathrm{T}}\Delta\lambda$ and $\Psi_{\mathrm{T}}\Delta\mu$, given by

$$\Delta C_{11} = \Delta M + \left(\frac{8\chi}{105} + \frac{4}{35}\right)\lambda\Delta\Psi_{\mathrm{N}} + \frac{1}{7}M\Delta\Psi_{\mathrm{N}} + \left(\frac{2\chi}{35g} - \frac{4}{35g}\right)\lambda\Delta\Psi_{\mathrm{T}} + \frac{2}{35g}M\Delta\Psi_{\mathrm{T}} \tag{B-6}$$

$$\Delta C_{12} = \Delta\lambda + \left(\frac{2\chi}{21} + \frac{22}{105}\right)\lambda\Delta\Psi_{\mathrm{N}} + \frac{1}{35}M\Delta\Psi_{\mathrm{N}} + \left(-\frac{1\chi}{35g} + \frac{2}{35g}\right)\lambda\Delta\Psi_{\mathrm{T}} - \frac{1}{35g}M\Delta\Psi_{\mathrm{T}} \tag{B-7}$$

$$\Delta C_{22} = \Delta M + \left(\frac{8\chi}{35} + \frac{8}{105}\right)\lambda\Delta\Psi_{\mathrm{N}} + \frac{1}{35}M\Delta\Psi_{\mathrm{N}} + \left(\frac{4\chi}{105g} - \frac{8}{105g}\right)\lambda\Delta\Psi_{\mathrm{T}} + \frac{4}{105g}M\Delta\Psi_{\mathrm{T}} \tag{B-8}$$

$$\Delta C_{44} = \Delta\mu - \frac{4g}{105}\mu\Delta\Psi_{\mathrm{N}} - \frac{2}{21}\mu\Delta\Psi_{\mathrm{T}} \tag{B-9}$$

$$\Delta C_{55} = \Delta\mu - \frac{4g}{35}\mu\Delta\Psi_N - \frac{16}{105}\mu\Delta\Psi_T \tag{B-10}$$

Appendix C. Derivation of the linearized PP-wave reflection coefficient

The polarization and slowness vectors of the incident P-wave and reflected P-wave are given by (Shaw and Sen, 2006)

$$\begin{aligned}
\mathbf{g}^{PP} &= [\sin\theta\cos\phi, \quad \sin\theta\sin\phi, \quad \cos\theta] \\
\mathbf{g}'^{PP} &= [-\sin\theta\cos\phi, \quad -\sin\theta\sin\phi, \quad \cos\theta] \\
\mathbf{p}^{PP} &= \left[\frac{\sin\theta\cos\phi}{\alpha}, \quad \frac{\sin\theta\sin\phi}{\alpha}, \quad \frac{\cos\theta}{\alpha}\right] \\
\mathbf{p}'^{PP} &= \left[-\frac{\sin\theta\cos\phi}{\alpha}, \quad -\frac{\sin\theta\sin\phi}{\alpha}, \quad \frac{\cos\theta}{\alpha}\right]
\end{aligned} \tag{C-1}$$

And the expressions of ξ^{PP} and η^{PP}_{mn} are listed as

$$\begin{aligned}
&\xi^{PP} = \cos 2\theta \\
&\eta^{PP}_{11} = \frac{\sin^4\theta\cos^4\phi}{\alpha^2},\ \eta^{PP}_{12} = \frac{\sin^4\theta\sin^2\phi\cos^2\phi}{\alpha^2}, \\
&\eta^{PP}_{13} = \frac{\sin^2\theta\cos^2\theta\cos^2\phi}{\alpha^2} \\
&\eta^{PP}_{22} = \frac{\sin^4\theta\sin^4\phi}{\alpha^2},\ \eta^{PP}_{23} = \frac{\sin^2\theta\cos^2\theta\sin^2\phi}{\alpha^2},\ \eta^{PP}_{33} = \frac{\cos^4\theta}{\alpha^2} \\
&\eta^{PP}_{44} = \frac{-4\sin^2\theta\cos^2\theta\sin^2\phi}{\alpha^2},\ \eta^{PP}_{55} = \frac{-4\sin^2\theta\cos^2\theta\cos^2\phi}{\alpha^2}, \\
&\eta^{PP}_{66} = \frac{4\sin^4\theta\sin^2\phi\cos^2\phi}{\alpha^2},\ \eta^{PP}_{21} = \eta^{PP}_{12},\ \eta^{PP}_{31} = \eta^{PP}_{13},\ \eta^{PP}_{32} = \eta^{PP}_{23}
\end{aligned} \tag{C-2}$$

Combining Eqs. (B-6)–(B-10), Eqs. (C-1)–(C-2), and Eq. (24), the scattering function S_{PP} can be derived as

$$\begin{aligned}
S_{PP} = {} & \Delta\rho\cos 2\theta + \frac{\sin^4\theta\cos^4\phi}{\alpha^2}\begin{bmatrix}\Delta M + \left(\frac{8\chi}{105}\lambda + \frac{4}{35}\lambda + \frac{1}{7}M\right)\Delta\Psi_N \\ + \left(\frac{2\chi}{35g}\lambda - \frac{4}{35g}\lambda + \frac{2}{35g}M\right)\Delta\Psi_T\end{bmatrix} \\
& + \frac{2\sin^4\theta\sin^2\phi\cos^2\phi}{\alpha^2}\begin{bmatrix}\Delta\lambda + \left(\frac{2\chi}{21}\lambda + \frac{22}{105}\lambda + \frac{1}{35}M\right)\Delta\Psi_N \\ + \left(-\frac{1\chi}{35g}\lambda + \frac{2}{35g}\lambda - \frac{1}{35g}M\right)\Delta\Psi_T\end{bmatrix} \\
& + \frac{2\sin^2\theta\cos^2\theta\cos^2\phi}{\alpha^2}\begin{bmatrix}\Delta\lambda + \left(\frac{2\chi}{21}\lambda + \frac{22}{105}\lambda + \frac{1}{35}M\right)\Delta\Psi_N \\ + \left(-\frac{1\chi}{35g}\lambda + \frac{2}{35g}\lambda - \frac{1}{35g}M\right)\Psi_T\end{bmatrix} \\
& + \frac{\sin^4\theta\sin^4\phi}{\alpha^2}\begin{bmatrix}\Delta M + \left(\frac{8\chi}{35}\lambda + \frac{8}{105}\lambda + \frac{1}{35}M\right)\Delta\Psi_N \\ + \left(\frac{4\chi}{105g}\lambda - \frac{8}{105g}\lambda + \frac{4}{105g}M\right)\Delta\Psi_T\end{bmatrix} \\
& + \frac{2\sin^2\theta\cos^2\theta\sin^2\phi}{\alpha^2}\begin{bmatrix}\Delta M + \left(\frac{8\chi}{35}\lambda + \frac{8}{105}\lambda + \frac{1}{35}M\right)\Delta\Psi_N \\ + \left(\frac{4\chi}{105g}\lambda - \frac{8}{105g}\lambda + \frac{4}{105g}M\right)\Delta\Psi_T - 2\left(\Delta\mu + \frac{4g}{105}\mu\Delta\Psi_N + \frac{2}{21}\mu\Delta\Psi_T\right)\end{bmatrix} \\
& + \frac{\cos^4\theta}{\alpha^2}\begin{bmatrix}\Delta M + \left(\frac{8\chi}{35}\lambda + \frac{8}{105}\lambda + \frac{1}{35}M\right)\Delta\Psi_N \\ + \left(\frac{4\chi}{105g}\lambda - \frac{8}{105g}\lambda + \frac{4}{105g}M\right)\Delta\Psi_T\end{bmatrix} - \frac{4\sin^2\theta\cos^2\theta\sin^2\phi}{\alpha^2}\begin{bmatrix}\Delta\mu + \frac{4g}{105}\mu\Delta\Psi_N \\ + \frac{2}{21}\mu\Delta\Psi_T\end{bmatrix} \\
& - \frac{4\sin^2\theta\cos^2\theta\cos^2\phi}{\alpha^2}\left[\Delta\mu + \frac{4g}{35}\mu\Delta\Psi_N + \frac{16}{105}\mu\Delta\Psi_T\right] \\
& + \frac{4\sin^4\theta\sin^2\phi\cos^2\phi}{\alpha^2}\left[\Delta\mu + \frac{4g}{35}\mu\Delta\Psi_N + \frac{16}{105}\mu\Delta\Psi_T\right]
\end{aligned} \tag{C-3}$$

Combining Eq. (C-3) and Eq. (23) yields

$$R_{PP}(\theta,\phi)=\frac{1}{4}\sec^2\theta\frac{\Delta M}{M}-2g\sin^2\theta\frac{\Delta\mu}{\mu}+\frac{1}{2}\left(1-\frac{\sec^2\theta}{2}\right)\frac{\Delta\rho}{\rho}$$
$$+\frac{1}{105}\left[\begin{array}{l}\left(16g^2\sin^2\theta+16g^2\tan^2\theta-14g\tan^2\theta\right)\sin^2\phi+\\ 24g^2\cos^2\theta+8g^2\tan^2\theta+\left(\frac{35}{4}-14g\right)\sec^2\theta-14g\end{array}\right]\Delta\Psi_N$$
$$+\frac{2g}{105}\left[\left(\tan^2\theta\sin^2\theta-5\sin^2\theta\right)\cos^2\phi-10\sin^2\theta+2\sec^2\theta\right]\Delta\Psi_T \quad \text{(C-4)}$$

References

Aiman, Y.A., Delorey, A.A., Lu, Y., Bokelmann, G., 2023. S_{Hmax} orientation in the Alpine region from observations of stress-induced anisotropy of nonlinear elasticity. Geophys. J. Int. 235, 2137–2148. https://doi.org/10.1093/gji/ggad353.

Aki, K., Richards, P.G., 1980. Quantitative Seismology: Theory and Methods. W.H. Freeman, San Francisco.

Angus, D.A., Verdon, J.P., Fisher, Q.J., Kendall, J.M., 2009. Exploring trends in microcrack properties of sedimentary rocks: an audit of dry-core velocity-stress measurements. Geophysics 74 (5), E193–E203. https://doi.org/10.1190/1.3183940.

Bakulin, A., Grechka, V., Tsvankin, I., 2000. Estimation of fracture parameters from reflection seismic data—Part II: fractured models with orthorhombic symmetry. Geophysics 65 (6), 1803–1817. https://doi.org/10.1190/1.1444864.

Bissantz, N., Dümbgen, L., Munk, A., Stratmann, B., 2008. Convergence analysis of generalized iteratively reweighted least squares algorithms on convex function spaces. J. Opt. 19 (4), 1828–1845. https://doi.org/10.1137/050639132.

Boness, N.L., Zoback, M.D., 2006. Mapping stress and structurally controlled crustal shear velocity anisotropy in California. Geology 34, 825–828. https://doi.org/10.1130/G22309.1.

Brown, R.J.S., Korringa, J., 1975. On the dependence of the elastic properties of a porous rock on the compressibility of the pore fluid. Geophysics 40 (4), 608–616. https://doi.org/10.1190/1.1440551.

Cao, H., Zhao, Y., Chen, H.C., Zhang, L.L., Cheng, G.X., Ji, D.T., Lu, L., 2025. Integrating well logs, 3D seismic, and earthquake data for comprehensive prediction of 3D in-situ stress orientations: A case study from the Weiyuan area in the Sichuan Basin, China. Pet. Sci. 22, 210–221. https://doi.org/10.1016/j.petsci.2024.07.015.

Chaudhry, N.A., 1995. Effects of aligned discontinuities on the elastic and transport properties of reservoir rocks. PhD Thesis, University of London.

Chen, F.B., Zong, Z.Y., 2022. PP-wave reflection coefficient in stress-induced anisotropic media and amplitude variation with incident angle and azimuth inversion. Geophysics 87 (6), C155–C172. https://doi.org/10.1190/geo2021-0706.1.

Chen, H.Z., Zhang, G.Z., Ji, Y.X., Yin, X.Y., 2017. Azimuthal seismic amplitude difference inversion for fracture weakness. Pure Appl. Geophys. 174, 279–291. https://doi.org/10.1007/s00024-016-1377-x.

Chen, F.B., Zong, Z.Y., Yin, X.Y., Stovas, A., 2023. Stress dependence of elastic wave dispersion and attenuation in fluid-saturated porous layered media. Sci. China Earth Sci. 66, 2622–2634. https://doi.org/10.1007/s11430-022-1147-7.

Chen, F.B., Zong, Y.H., Yin, X.Y., 2024. Seismic scattering inversion for multiple parameters of overburden-stressed isotropic media. Geophysics 89 (6), T319–T336. https://doi.org/10.1190/geo2023-0636.1.

Far, M.E., Sayers, C.M., Thomsen, L., Han, D.H., Castagna, J.P., 2013. Seismic characterization of naturally fractured reservoirs using amplitude versus offset and azimuth analysis. Geophys. Prospect. 61 (2), 427–447. https://doi.org/10.1111/1365-2478.12011.

Griffiths, L., Heap, M.J., Baud, P., Schmittbuhl, J., 2017. Quantification of microcrack characteristics and implications for stiffness and strength of granite. Int. J. Rock Mech. Min. Sci. 100, 138–150. https://doi.org/10.1016/j.ijrmms.2017.10.013.

Gurevich, B., Makarynska, D., de Paula, O.B., Pervukhina, M., 2010. A simple model for squirt-flow dispersion and attenuation in fluid saturated granular rocks. Geophysics 75 (6), N109–N120. https://doi.org/10.1190/1.3509782.

Gurevich, B., Pervukhina, M., Makarynska, D., 2011. An analytic model for the stress-induced anisotropy of dry rocks. Geophysics 76 (3), WA125–WA133. https://doi.org/10.1190/1.3567950.

Han, D.H., Nur, A., Morgan, D., 1986. Effects of porosity and clay content on wave velocities in sandstones. Geophysics 51 (11), 2093–2107. https://doi.org/10.1190/1.1442062.

Heidbach, O., Rajabi, M., Cui, X., et al., 2018. The world stress map database release 2016: crustal stress pattern across scales. Tectonophysics 744, 484e498. https://doi.org/10.1016/j.tecto.2018.07.007.

Hill, R., 1952. The elastic behaviour of a crystalline aggregate. Proc. Phys. Soc. 65, 349–354. https://doi.org/10.1088/0370-1298/65/5/307.

Hornby, B.E., Schwartz, L.M., Hudson, J.A., 1994. Anisotropic effective-medium modeling of the elastic properties of shales. Geophysics 59 (10), 1570–1583. https://doi.org/10.1190/1.1443546.

Hudson, J.A., 1981. Wave speeds and attenuation of elastic waves in material containing cracks. Geophys. J. Int. 64 (1), 133–150. https://doi.org/10.1111/j.1365-246X.1981.tb02662.x.

Johnson, P.A., Rasolofosaon, P.N.J., 1996. Nonlinear elasticity and stress-induced anisotropy in rock. J. Geophys. Res. Solid Earth 101, 3113–3124. https://doi.org/10.1029/95JB02880.

Kuster, G.T., Toksöz, M.N., 1974. Velocity and attenuation of seismic waves in two-phase media: part I. Theoretical formulations. Geophysics 39 (5), 587–606. https://doi.org/10.1190/1.1440450.

Li, W.Q., Hu, H.S., 2023. Reflection and transmission of plane waves in stressed media with an imperfectly bonded interface. Geophys. J. Int. 233, 2233–2253. https://doi.org/10.1093/gji/ggad037.

Li, K., Yin, X.Y., Zong, Z.Y., Lin, H.K., 2020. Seismic AVO statistical inversion incorporating poroelasticity. Pet. Sci. 17 (5), 1237–1258. https://doi.org/10.1007/s12182-020-00483-5.

Li, S.Q., Wang, W.H., Su, Y.D., Guo, J.X., 2023. Effective elastic properties and S-wave anisotropy for rocks containing any oriented penny-shaped cracks in transversely isotropic background. Geophysics 88 (3), MR65–MR81. https://doi.org/10.1190/geo2022-0388.1.

Liu, E., Martinez, A., 2014. Seismic Fracture Characterization: Concepts and Practical Applications. EAGE Publications. https://doi.org/10.3997/9789073834507.

Liu, J.X., Cui, Z.W., Wang, K.X., 2009. The relationships between uniaxial stress and reflection coefficients. Geophys. J. Int. 179, 1584–1592. https://doi.org/10.1111/j.1365-246X.2009.04353.x.

Liu, J.X., Cui, Z.W., Wang, K.X., 2012. Effect of stress on reflection and refraction of plane wave at the interface between fluid and stressed rock. Soil Dynam. Earthq. Eng. 42, 47–55. https://doi.org/10.1016/j.soildyn.2012.05.022.

Lyu, F., Liu, J.P., Chen, L., Tao, B.C., Liu, X.Y., 2024. 3D in-situ stress prediction for shale reservoirs based on the CapsNet-BiLSTM hybrid model. Int. J. Rock Mech. Min. Sci. 183, 105937. https://doi.org/10.1016/j.ijrmms.2024.105937.

Ma, Z.Q., Yin, X.Y., Li, K., Tan, Y.Y., 2022. Fourier coefficients variation with angle for fracture detection and fluid discrimination in tilted transversely isotropic media. Surv. Geophys. 43, 775–813. https://doi.org/10.1007/s10712-022-09704-5.

Maupin, V., Park, J., Romanowicz, B., Dziewonski, A., 2007. Theory and observations – wave propagation in anisotropic media. Treat. Geophys. 1, 289–321. https://doi.org/10.1016/b978-044452748-6.00007-9.

Mavko, G., Mukerji, T., Godfrey, N., 1995. Predicting stress-induced velocity anisotropy in rocks. Geophysics 60 (4), 1081–1087. https://doi.org/10.1190/1.1443836.

Nur, A., Simmons, G., 1969. Stress-induced velocity anisotropy in rock: an experimental study. J. Geophys. Res. 74, 6667–6674. https://doi.org/10.1029/JB074i027p06667.

Pan, X.P., Zhao, Z.Z., 2024. A decoupled fracture- and stress-induced PP-wave reflection coefficient approximation for azimuthal seismic inversion in stressed horizontal transversely isotropic media. Surv. Geophys. 45, 151–182. https://doi.org/10.1007/s10712-023-09791-y.

Pan, X.P., Lu, C.X., Zhao, Z.Z., Liu, J.X., 2024. Characteristics of orthorhombic anisotropic seismic response induced by horizontal in situ stress in vertical transversely isotropic media. Sci. China Earth Sci. 67 (7), 2291–2310. https://doi.org/10.1007/s11430-023-1294-4.

Pastori, M., Piccinini, L., Margheriti, L., Improta, L., Valoroso, L., Chiaraluce, L., Chiarabba, C., 2009. Stress aligned cracks in the upper crust of the Val d'Agri region as revealed by shear wave splitting. Geophys. J. Int. 179, 601–614. https://doi.org/10.1111/j.1365-246X.2009.04302.x.

Pšenčík, I., Martins, J.L., 2001. Properties of weak contrast PP reflection/transmission coefficients for weakly anisotropic elastic media. Studia Geophys. Geod. 45, 176–199. https://doi.org/10.1023/A:1021868328668.

Rüger, A., 1997. P -wave reflection coefficients for transversely isotropic models with vertical and horizontal axis of symmetry. Geophysics 62 (3), 713–722. https://doi.org/10.1190/1.1444181.

Sarkar, D., Bakulin, A., Kranz, R., 2003. Anisotropic inversion of seismic data for stressed media: Theory and a physical modeling study on Berea Sandstone. Geophysics 68 (2), 690–704. https://doi.org/10.1190/1.1567240.

Sayers, C.M., 2002. Stress-dependent elastic anisotropy of sandstones. Geophys. Prospect. 50, 85–95. https://doi.org/10.1046/j.1365-2478.2002.00289.x.

Sayers, C.M., Kachanov, M., 1995. Microcrack-induced elastic wave anisotropy of brittle rocks. J. Geophys. Res. 100, 4149–4156. https://doi.org/10.1029/94jb03134.

Sayers, C.M., Leaney, W.S., Bratton, T.R., 2024. Stress-induced anisotropy in Gulf of Mexico sandstones and the prediction of in situ stress. Geophys. Prospect. 72, 1852–1864. https://doi.org/10.1111/1365-2478.13497.

Shapiro, S., Kaselow, A., 2005. Porosity and elastic anisotropy of rocks under tectonic stress and pore-pressure changes. Geophysics 70 (5), N27–N38. https://doi.org/10.1190/1.2073884.

Sharma, M.D., 2007. Effect of initial stress on reflection at the free surface of anisotropic elastic medium. J. Earth Syst. Sci. 116, 537–551. https://doi.org/10.1007/s12040-007-0049-8.

Shaw, R.K., Sen, M.K., 2006. Use of AVOA data to estimate fluid indicator in a vertically fractured medium. Geophysics 71 (3), C15–C24. https://doi.org/10.1190/1.2194896.

Sheikholeslami, M.R., Parisa, M., Hamid, R.J., Ghassemi, M.R., 2021. Stress field and tectonic regime of Central Iran from inversion of the earthquake focal

mechanisms. Tectonophysics 813, 228931. https://doi.org/10.1016/j.tecto.2021.228931.
Thomsen, L., 1986. Weak elastic anisotropy. Geophysics 51 (10), 1954–1966. https://doi.org/10.1190/1.1442051.
Wang, P., Chen, X.H., Li, J.Y., Wang, B.F., 2020. Accurate porosity prediction for tight sandstone reservoir: A case study from North China. Geophysics 85, B35–B47. https://doi.org/10.1190/GEO2018-0852.1.
Wang, P., Cui, Y.A., Liu, J.X., 2022. Fluid discrimination based on inclusion-based method for tight sandstone reservoirs. Surv. Geophys. 43, 1469–1496. https://doi.org/10.1007/s10712-022-09712-5.
Wood, A., 1955. A textbook of sound, 11. McMillan Co. Phys. Today 9, New York, p. 37. https://doi.org/10.1063/1.3059819.
Zong, Z.Y., Ji, L.X., 2021. Model parameterization and amplitude variation with angle and azimuthal inversion in orthotropic media. Geophysics 86 (1), R1–R14. https://doi.org/10.1190/GEO2018-0778.1.
Zong, Z.Y., Yin, X.Y., Wu, G.C., 2015. Geofluid discrimination incorporating poroelasticity and seismic reflection inversion. Surv. Geophys. 36 (5), 659–681. https://doi.org/10.1007/s10712-015-9330-6.